

Modelling and Experimental Investigation of an Integrated Optical Microheater in SOI

A THESIS

submitted by

SAKET KAUSHAL

for the award of the degree

of

MASTER OF SCIENCE

(by Research)



**Department of Electrical Engineering
INDIAN INSTITUTE OF TECHNOLOGY MADRAS**

April 2016

THESIS CERTIFICATE

This is to certify that the thesis titled **Modelling and Experimental Investigation of an Integrated Optical Microheater in SOI**, submitted by **Saket Kaushal**, to the Indian Institute of Technology, Madras, for the award of the degree of **Master of Science**, is a bonafide record of the research work done by him under my supervision. The contents of this thesis, in full or in parts, have not been submitted to any other Institute or University for the award of any degree or diploma.

Dr. Bijoy Krishna Das
Research Guide
Associate Professor
Dept. of Electrical Engineering
IIT-Madras, 600 036

Place: Chennai

Date: 25th April 2016

Dedicated to my Parents

ACKNOWLEDGEMENTS

First and foremost, I would like to express my gratitude towards my research supervisor, Dr Bijoy Krishna Das. His guidance throughout my stay at IITM has been instrumental in shaping up this work. I would also take this opportunity to thank all the faculty members who have taught me here.

Integrated Optoelectronics Group has been like a family to me. Unlike other groups, absence of hierarchy here helped in fruitful interactions between senior research scholars and newbies. I would personally thank Meenu and Sujith for teaching me fabrication and characterization steps. Their experience is invaluable. I got lot of help and inputs from Sarath on COMSOL simulations. I am thankful to him. I wish Shantanu, Parimal, Riddhi, Sumi, Ramesh, Srivatsa, Usmaan, and Srinath all the very best in their present and future endeavors. I would also like to thank group alumni: Sakthivel, Karthik, Varun, Harish, Chaitanya, Dadavali, Vivek, Mandar, Sireesha, Rashmi, Sidharth, Mani Teja, Dipak for their valuable inputs and feedback all throughout my tenure.

I must acknowledge the fabrication facilities and working ambiance available in Microelectronics Lab and newly established Centre for NEMS and Nanophotonics at IIT Madras, which played a vital role for my hands-on/learning various fabrication processes and of course to execute my MS research work. I am grateful to technical staff Mr. Rajendran, Prakash, and Sridhar, they ensured proper maintenance and smooth functioning of lab equipment and facilities.

I am and always will be indebted to my parents. They have been pillars of unwavering support for me in testing times. I look up to them for their wisdom and experience.

ABSTRACT

The CMOS fabrication compatibility of waveguide devices and the presence of strong thermo-optic effect makes silicon-on-insulator (SOI) an attractive platform for large scale integration of reconfigurable optical systems viz. routers, switches, filters, delay lines etc. Integrated optical microheaters are used for local reconfiguration/correction of phase-sensitive devices via thermo-optic effect. However, high thermal sensitivity of resonance devices ($d\lambda_r/dT \sim 100$ pm/K) leads to thermal crosstalk, especially for densely packed large-scale integrated optical circuits in SOI platform. It is therefore, important to investigate the temperature distribution and effective control of thermo-optic phase-shift by a microheater integrated with waveguide structures. A linear piece-wise model has been formulated to analyse the performance of a metallic microheater integrated with single-mode waveguides ($\lambda \sim 1550$ nm) in silicon-on-insulator (SOI). The model has been used to evaluate integrated optical microheaters fabricated in a SOI substrate with $2\text{-}\mu\text{m}$ device layer thickness. Fabry-Perot modulation technique has been used to extract the effective thermo-optic phase-shift and response time. The effective thermal power budget of $P_{eff,\pi} \sim 500$ μW for a π phase-shift and a switching time of $\tau \sim 9$ μs , have been recorded for a typical Ti heater stripe of length $L_H = 50$ μm , width $W_H = 2$ μm , and thickness $t_H \sim 150$ nm; integrated with a Fabry-Perot waveguide cavity of length ~ 20 μm . It has been shown that the performance of a heater improves (in terms of power budget) as the length of a microheater decreases. However, smaller heater-size requires higher joule heating to obtain a desired phase-shift which is again found to be dependent on polarization of the guided mode because of thermal stress.

TABLE OF CONTENTS

ACKNOWLEDGEMENTS	ii
ABSTRACT	iii
LIST OF TABLES	vi
LIST OF FIGURES	x
ABBREVIATIONS	xi
NOTATION	xiv
1 INTRODUCTION	1
1.1 Motivation	1
1.2 Research Objective	4
1.3 Thesis Organization	4
2 THERMO-OPTIC DETUNING: A QUANTITATIVE ANALYSIS	5
2.1 CROW Structure: Case Study	5
2.1.1 Design Principle	6
2.1.2 Maximally Flat 8-bit Delay-Line in SOI	9
2.2 Fabrication Induced Disorder and Thermo-optic Compensation	12
2.3 Reconfigurable Delay lines	14
2.4 Conclusions	16

3	AN INTEGRATED OPTICAL MICROHEATER : THEORETICAL STUDY	17
3.1	Design and Modelling	17
3.2	Transient Analysis	25
3.3	Conclusions	26
4	EXPERIMENTAL INVESTIGATIONS	28
4.1	Mask Design for Device Fabrication	28
4.2	Device Fabrication	30
4.2.1	Waveguide Loss and Mode Profile Measurement	35
4.2.2	Sheet Resistance Measurement	38
4.3	Results and Discussion	39
4.3.1	Static Microheater Response	39
4.3.2	Investigation of Polarization Rotation	44
4.3.3	Transient Response	45
4.4	Conclusions	46
5	CONCLUSIONS	47
5.1	Summary	47
5.2	Future scope of work	48
A	FABRICATION CHEMISTRY	50
A.1	Chromium Etchant	50
A.2	Aluminum Etchant	50

LIST OF TABLES

3.1	Calculated L_{eff} of a Ti thinfilm microheater design (as shown in Figure 3.1) values for different L_H for $W = 1.4 \mu\text{m}$, $h = 1.5 \mu\text{m}$, $H = 2 \mu\text{m}$, $W_H = 2 \mu\text{m}$, $S = 3 \mu\text{m}$, $t_H = 150 \text{ nm}$	24
3.2	Calculated L_{eff} of a Ti thin film microheater design (as shown in Figure 3.1) values for different L_H for $W = 500 \text{ nm}$, $h = 75 \text{ nm}$, $H = 250 \text{ nm}$, $W_H = 2 \mu\text{m}$, $S = 3 \mu\text{m}$, $t_H = 150 \text{ nm}$	24
4.1	SOI wafer specifications	30
4.2	Optimized etching parameters.	32

LIST OF FIGURES

1.1	Schematic of a 1X2 thermo-optic switch consisting of top clad based microheater with air trenches on one arm of the switch. Based on applied bias, power is switched from one output port to the other port[24].	2
1.2	Schematic of a 2X2 symmetric thermo-optic switch with adiabatic bends to ensure delocalised modes and low loss integration of heaters on silicon [38].	3
2.1	(a) Scheme of a single ring resonator operating in all-pass-filter configuration, (b) Schematic of a reflecting CROW with N identical ring resonators; a_n and b_n are incident and reflected field amplitude and r_n is the reflection coefficient at n^{th} designated coupler.	7
2.2	(a) Normalized transmission of micro ring resonator with a typical photonic wire waveguide (W=450 nm, H=250 nm) in SOI, with ring radius 25 μm , $r_0 = 0.995$, $\alpha = 3$ db/cm (b) Corresponding group delay versus wavelength.	7
2.3	(a) Optimized inter-ring coupling coefficients for 2^{nd} , 4^{th} , 6^{th} , 8^{th} order CROWs for 8 bit maximally flat delay response. (b) Relation between coupling coefficient κ and spacing S for coupling length $L_c = 10 \mu\text{m}$ for the directional coupler consisting of photonic wire waveguides as shown in inset.	10
2.4	(a) Group delay vs wavelength (around a DWDM channel) for different order CROWs; (b) Extracted optimized separations between coupled waveguides shown in ascending order separately for 2^{nd} , 4^{th} , 6^{th} , 8^{th} order CROWs.	10
2.5	(a) Schematic of six CROW structure with ring radius of 97 μm and straight coupling section of 10 μm [denoted by $C_1, C_2 \dots C_6$]; (b) Cross-section of directional coupler with spacing S between single mode photonic wire waveguides. (c) Six coupling coefficients and corresponding spacing between coupled waveguides (apodized in ascending order) of 6^{th} order maximally flat CROW based delay line.	11

2.6	Fabrication induced disorder in 6^{th} order maximally flat delay line: Black trace shows the ideal response when there is no fabrication imperfection across the ring resonators, red trace shows the degraded response when a probabilistic variation of 2 nm in waveguide width is considered across all the ring resonators.	12
2.7	(a) Schematic of cross section of rib waveguide in SOI where H is rib height, h is slab height, W is width of waveguide. (b) Plot shows the dependence of n_{eff} on W for different h for a photonic wire rib waveguide of $H = 250$ nm.	13
2.8	Variable power splitter driven by a transverse temperature gradient [59].	14
2.9	(a) Micrograph of series coupled microring resonators integrated with microheaters for tunable delay. (b) Mechanism of tuning of delay by selectively turning on ring resonators using microheaters based phase shifters. (c) Measured group delay and insertion loss for increasing number of rings in resonance [34].	15
3.1	Top and cross-section views of a simple microheater design integrated with a single-mode SOI rib waveguide (width W , rib height H , slab height h). L_H and W_H are the heater length and width, respectively. .	18
3.2	Calculated electric field profiles for a single-mode SOI rib waveguide with $H = 2 \mu\text{m}$, $W = 1.4 \mu\text{m}$ and $h = 1.5 \mu\text{m}$: (a) E_y component for TE-polarization, and (b) E_z component for TM polarization. The microheater shown in yellow-strip is kept at a separation of $3 \mu\text{m}$ from rib edge to avoid overlap with the guided fields.	19
3.3	Simulated top and cross-section (across the dotted line) temperature profile of the microheater (Ti stripe with $W_H = 2 \mu\text{m}$, $L_H = 50 \mu\text{m}$, $t_H = 150$ nm, $S = 3 \mu\text{m}$): (a) Integrated with rib waveguide ($W = 1.4 \mu\text{m}$, $H = 2 \mu\text{m}$, $h = 1.5 \mu\text{m}$) for an applied bias of $i_H = 0.9$ mA. (b) Integrated with rib waveguide ($W=500$ nm, $H=250$ nm, $h = 0.075$ nm) for an applied bias of $i_H = 0.9$ mA.	20
3.4	(a) Temperature distributions along the waveguide for $L_H = 50 \mu\text{m}$, for different applied current i_H for ($W = 1.4 \mu\text{m}$, $H = 2 \mu\text{m}$, $h = 1.5 \mu\text{m}$). (b) Normalized temperature distribution and piecewise linear model plotted as a function of distance along the waveguide.	22
3.5	(a) Dependence of slope m on slab height h . (b) Variation of offset α as a function of L_H	23

3.6	(a) Simulated transient response of micron cross section waveguide ($W = 1.4 \mu\text{m}$ and $h = 1.5 \mu\text{m}$) with Ti micro heater ($W_H = 2 \mu\text{m}$, $t_H = 150 \text{ nm}$, $L_H = 200 \mu\text{m}$); T_{rise} (T_{fall}) = $4.3 \mu\text{s}$ ($4.4 \mu\text{s}$). (b) Simulated transient response of sub micron cross section waveguide ($W = 500 \text{ nm}$ and $h = 75 \text{ nm}$) with Ti micro heater ($W_H = 2 \mu\text{m}$, $t_H = 150 \text{ nm}$, $L_H = 200 \mu\text{m}$); T_{rise} (T_{fall}) = $7.8 \mu\text{s}$ ($9 \mu\text{s}$). Black dotted trace shows the input square pulse ($V_H(t)$) with 50 % duty cycle and frequency 20 KHz. . .	25
3.7	(a) Cross-section of $2 \mu\text{m}$ SOI ($W = 1.4 \mu\text{m}$ and $h = 1.5 \mu\text{m}$) with Ti micro heater ($W_H = 2 \mu\text{m}$, $t_H = 150 \text{ nm}$). (b) Cross-section of 250 nm SOI ($W = 500 \text{ nm}$ and $h = 75 \text{ nm}$) with Ti micro heater ($W_H = 2 \mu\text{m}$, $t_H = 150 \text{ nm}$).	26
4.1	Combined mask layout of microheaters along with probe pads (blue) integrated with rib waveguides (red).	29
4.2	Schematic of mask layout of microheaters integrated with rib waveguides: A total of 36 waveguides (grey) were defined, out of which 6 were reference waveguides and rest were integrated with microheaters (yellow) and contact pads (white).	30
4.3	Fabrication process flow of microheaters integrated with rib waveguides.	31
4.4	Confocal image showing Titanium remnants on waveguide due to non conformal coating of thinner resist S1805 on top of waveguide.	33
4.5	Confocal image of Ti microheaters integrated with waveguides after Titanium lift off, black spots (circled in red) correspond to Titanium flakes. Waveguide, microheaters and probe pads are labeled accordingly	34
4.6	(a) Photograph of microheaters of different L_H integrated with rib waveguides. (b) Zoomed Confocal micrograph of a microheater with $L_H = 100 \mu\text{m}$, $W_H = 2 \mu\text{m}$. (c) SEM image of polished end-facet of waveguide with typical width and etch depth measured. Image clearly shows the cross-section of $2 \mu\text{m}$ SOI.	35
4.7	Measured normalized transmission characteristics of a waveguide for TE polarization as a function of wavelength around 1570 nm	37
4.8	(a) Measured Mode profile for TE polarization, Mode size is $6.1 \mu\text{m} \times 2.6 \mu\text{m}$. (b) Measured Mode profile for TM polarization, Mode size is $5.7 \mu\text{m} \times 2.6 \mu\text{m}$	38

4.9	(a) Free space characterization setup used to test microheaters integrated with rib waveguides. (b) Zoomed in photograph of the characterization setup showing DUT with electrical probes at the centre and i/o objective lenses controlled with pico actuators at either side.	40
4.10	(a) Calculated intensity modulated output as function of $\Delta\phi$ for a waveguide cavity of length 20 mm with propagation loss of 1 dB/cm for TE-polarization at $\lambda = 1570$ nm. (b) Experimentally obtained intensity modulated output (TE-polarization at $\lambda = 1570$ nm) as a function of current (i_H) through a heater with $L_H = 100 \mu\text{m}$ and $W_H = 2 \mu\text{m}$	42
4.11	(a) Effective electrical power (P_{eff}) versus induced phase change ($\Delta\phi$) in the waveguide for $W_H = 2 \mu\text{m}$, and different L_H viz. 50 μm , 100 μm , 200 μm for TE (solid line) and TM (dotted line) polarized light. (b) Peak temperature change (δT_p) required as a function of desired phase change of the guided mode. (c) Effective electrical power (P_{eff}) versus induced phase change ($\Delta\phi$) in the waveguide for $W_H = 2 \mu\text{m}$ (solid line) and $W_H = 3 \mu\text{m}$ (dotted line), and different L_H viz. 50 μm , 100 μm , 200 μm for TE polarized light.	43
4.12	Throughput transmission as a function of current of a waveguide with slab deposited microheater with TE polarized light as input: (a) Output polarizer set to pass TE polarized light (b) Output polarizer set to pass TM polarized light.	44
4.13	Transient response : Measured output response of microheater with $W_H = 2 \mu\text{m}$ and $L_H = 200 \mu\text{m}$ (blue trace) to a 10 kHz drive signal (yellow trace). Average response time is $\tau_{\text{resp}} \sim 9 \mu\text{s}$	45

ABBREVIATIONS

APF	All Pass Filter
AWG	Array Waveguide Grating
BOX	Buried Oxide
CCD	Charge Coupled Device
CMOS	Complementary Metal Oxide Semiconductor
CROW	Coupled Resonator Optical waveguide
DWDM	Dense Wavelength Division Multiplexing
DI	De-Ionised
DUT	Device Under Test
DSO	Digital Storage Oscilloscope
FOM	Figure of Merit
FSR	Free Spectral Range
ICP	Inductively Coupled Plasma
i-line	Ultra Violet radiation of wavelength ~ 365 nm
MZI	Mach Zehdner Interferometer
PEB	Post Exposure Bake
PhC	Photonic Crystals
PC	Polarization Controller
P	Polarizer
PPR	Positive Photoresist
RIE	Reactive Ion Etching
SOI	Silicon on Insulator

SMF	Single Mode Fiber
SEM	Scanning Electron Microscope
TE	Transverse Electric
TM	Transverse Magnetic
UV	Ultra Violet
WDM	Wavelength Division Multiplexing

Units

$\mu\text{m}/\text{min}$	micrometer per minute (etch rate)
dB	Decibel (logarithmic power or amplitude ratio)
dBm	Decibel milliWatts (logarithmic power)
μm	micrometer (length)
mTorr	milliTorr (pressure)
mW	milliWatt (power)
mW/cm^2	milliWatt per square centimetre (UV light intensity)
rpm	revolutions per minute (spin speed)
sccm	standard cubic centimeter per minute (gas flow)
pJ/bit	picoJoules/bit (Energy penalty)
μs	microsecond (Response time)
K^{-1}	Per unit Kelvin (Thermo optic coefficient)

Chemicals

CH₃COOH	Acetic Acid
Al	Aluminum
ACN	Ammonium Ceric Nitrate
Ar	Argon
Cr	Chromium
HF	Hydroflouric Acid
IPA	Isopropyl Alcohol
HNO₃	Nitric Acid
Pt	Platinum
Si	Silicon
SiO₂	Silicon Dioxide
SF₆	Sulphur Hexaflouride
H₃PO₄	OrthoPhosphoric Acid
TMAH	Tetra Methyl Ammonium Hydroxide
Ti	Titanium
TCE	Trichloroethylene

NOTATION

λ	Wavelength
λ_r	Resonant Wavelength
α	Propagation loss
H	Rib Height
h	Slab Height
W	Waveguide Width
W_H	Heater Width
L_H	Heater Length
t_H	Heater thickness
L_C	Coupler length
i_H	Applied current
S	Separation between waveguide edge and heater edge
L_{eff}	Effective heater length
δT_p	Peak temperature change
$f(x)$	Characteristic Distribution function
$H(x)$	Heaviside step function
n_{eff}	Effective index
P_π	Switching power
$\frac{dn}{dT}$	Thermo-optic coefficient
T_{rise}	Rise Time
T_{fall}	Fall Time
τ_{resp}	Response Time
r	Reflection coefficient
κ	Coupling coefficient
ϕ	Phase
f	Loading factor
B_N	Bessel's polynomial of order N
R_F	Fresnel reflectivity
L	Fabry Perot cavity length
ζ	Extinction ratio
R_i	Line resistance
R_{eff}	Effective resistance

i_H	Current through microheater
P_{eff}	Effective electrical power
P_T	Throughput power

CHAPTER 1

INTRODUCTION

This thesis is about theoretical and experimental investigations of an integrated optical microheater for silicon photonics applications. In this introductory chapter, motivation behind the work, original research objective and organization of the thesis have been briefly discussed.

1.1 Motivation

In last decade or so, phenomenal activity has been reported in the area of silicon photonics. Stand alone devices such as MUX/de-MUXs [1, 2], filters [3, 4], lasers [5, 6, 7], photodetectors [8], modulators [9, 10] have been successfully demonstrated. Silicon on insulator platform has shown lot of promise in sensing [11, 12] and spectroscopy [13] based applications as well.

Silicon photonics is the dominant platform for on-chip optical interconnects. Recently, a electronic-photonic system was demonstrated on a single silicon chip, integrating close to a billion transistors and hundreds of photonic components working in tandem to realize a microprocessor, consuming only 1.3 pJ/bit energy to transmit data on-chip from one point to other [14]. This achievement has heralded a new era of next generation computing and communication systems where the appetite for power and bandwidth is growing exponentially [15]. Exploiting state of the art CMOS manufacturing processes, photonic components can be integrated on the same platform along side transistors with

high yield [16, 17, 18, 19]. Large refractive index contrast of silicon with silica/air enables tight confinement of guided modes. Active control of guided modes is possible via strong plasma dispersion and thermo-optic effects [20].

Plasma dispersion effect is mainly used to demonstrate high speed modulators [21, 22], switches [23] etc. However, large thermo-optic coefficient of Silicon ($dn/dT \sim 1.86 \cdot 10^{-4} K^{-1}$) is frequently used for an energy efficient switching [24, 25, 26, 27], routing [28, 29, 30], tuning [31], reconfigurable circuits [32, 33, 34, 35] etc. Thermo-optic effect, albeit inherently slower compared to plasma dispersion effect is essentially lossless leading to huge prospects in optical interconnect and microwave photonics applications [36, 37]. Large thermo-optic coefficient of silicon leads to high thermal sensitivity of silicon based circuits. However, one can take advantage of this effect by integrating phase shifter for localized tuning of phase error due to fabrication imperfections and for reconfigurable operation of large scale circuits viz delay lines, filters etc. Joule heating effect is most commonly used to achieve thermo-optic modulation in Silicon. Most of the instances of thermo-optic switches are based on over-clad heaters [39, 40]

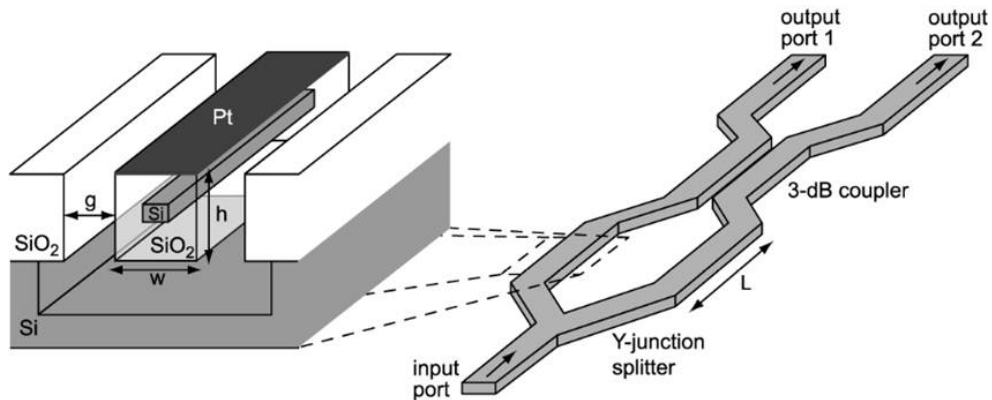


Figure 1.1: Schematic of a 1X2 thermo-optic switch consisting of top clad based micro-heater with air trenches on one arm of the switch. Based on applied bias, power is switched from one output port to the other port[24].

where in high resistance metal is deposited on top of buried waveguide as shown in Figure 1.1. A 1X2 thermo optic switch with Pt deposited on top of silica clad waveguide on

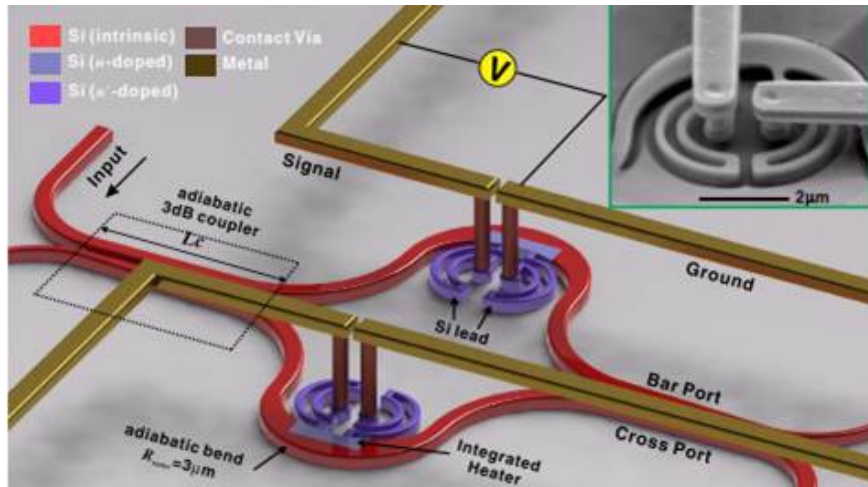


Figure 1.2: Schematic of a 2X2 symmetric thermo-optic switch with adiabatic bends to ensure delocalised modes and low loss integration of heaters on silicon [38].

one of the arms of switch is shown here. Applying bias on Pt heater enables switching of power from one port to other. Undercut trenches helps in trapping heat within silicon core ensuring low switching power (P_{π}). But trapping of heat within silicon core due to trenches has a downside. It leads to high response time ($\tau_{res} \sim 150 \mu s$) as it takes longer time for heat to diffuse out of the core.

On the other hand, in lateral heaters [41, 38] metal is deposited directly on slab region adjacent to rib waveguide (Figure 1.2), ensuring better usage of thermal energy. Moreover, slab forms a conductive path to dissipate heat faster, leading to lower response time as well ($\tau_{res} < 10 \mu s$). As seen in Figure 1.2 lightly doped silicon is used as a resistive heater, heating the waveguide core directly. Arms of the MZI is widened adiabatically to connect to low resistance silicon leads. But, high thermal sensitivity of Silicon ($d\lambda_0/dT \sim 100 \text{ pm/K}$) leads to thermal crosstalk in these slab deposited heaters, especially for large scale tightly packed circuits.

There have been attempts in recent past to model and analyze microheater based active photonic devices - mostly their tunability, bandwidth and temporal responses, etc. using finite element method (FEM) based numerical simulations [42, 43, 44, 45, 46, 47]. But,

there is no analytical and/or empirical working model available in the literature so that an integrated optical phase-shifter can be designed and evaluated directly to estimate the effective length/area of the microheater which is not only crucial for reducing overall power budget, but more importantly enable circuit designers to design large scale photonic interconnects with lower thermal crosstalks.

1.2 Research Objective

As it appears, thermal crosstalk is a major bottleneck in large scale integration of reconfigurable devices in SOI platform. Theoretical model of a microheater needs to be developed to obtain the temperature distribution in an integrated optical chip. In this work, it was proposed to simulate performance of a typical thermo-optic phase shifter numerically to develop an empirical temperature distribution model and its validation with experimental results.

1.3 Thesis Organization

The entire thesis work has been presented in three distinct chapters excluding Chapter 1 for Introduction and Chapter 5 for Conclusions.

Chapter 2 discusses a case study of maximally flat delay lines using Coupled Ring Optical Waveguides, fabrication imperfection induced disorder in response is also studied. Local correction of phase error and reconfigurable operation using thermo-optic tuning is discussed. Chapter 3 explores the design of slab deposited microheaters and formulation of linear piece model to estimate temperature distribution along the waveguide due to applied bias on microheater. Chapter 4 presents the optimized fabrication process steps of microheaters and concludes with characterization results.

CHAPTER 2

THERMO-OPTIC DETUNING: A QUANTITATIVE ANALYSIS

Utilizing large thermo-optic coefficient of silicon, microheaters based phase shifters can be used to locally tune the phase error incurred due to fabrication imperfections. Moreover, phase shifters are used in reconfigurable large scale circuits such as delay lines. To assess thermal crosstalk and impact of fabrication induced phase error in output response; a case study of maximally flat delay lines using Coupled Ring Optical Waveguides (CROWs) is undertaken. Design principle employed in extracting inter-ring coupling coefficients is discussed in detail. Fabrication induced disorder in delay response is also studied. Finally, it is qualitatively discussed how a suitably designed integrated optical microheater can be employed not only for phase error correction but also for tunable and/or reconfigurable on-chip delay lines.

2.1 CROW Structure: Case Study

Applications of delay lines include but are not limited to accurate synchronization for bit level processing [48], signal equalization, optical filtering and dispersion compensation, optical buffer memories [49], phased arrays etc. Photonic crystals (PhCs) and coupled resonator optical waveguides (CROW) are two commonly used approaches for the design of optical delay line in silicon-on-insulator (SOI) platform [50]. PhCs are known for slowing down light drastically but are prone to high extrinsic losses [51].

Moreover, design and fabrication of a tunable delay-line using PhC resonance structures remain extremely challenging. CROWs, on the other hand provide tunable low loss structures to effectively slow down light over a wide bandwidth [52]. Optimization of delay lines need proper tailoring of coupling coefficients between successive rings. In the next section we design 8 bit maximally flat delay line in SOI using series coupled ring optical waveguides. Coupling coefficients between successive rings are extracted by employing concepts from analog filters. Fabrication induced disorder in delay response is also studied.

2.1.1 Design Principle

The scheme of all-pass filter with a single ring is shown in Figure 2.1a and its transfer function can be derived as [53]:

$$\frac{E_o}{E_i} = \frac{r_0 - ae^{i\phi}}{1 - r_0ae^{i\phi}} \quad (2.1)$$

Where $\phi = \beta L = \frac{2\pi\nu}{FSR} = 2\pi(m + \frac{\Delta\nu}{FSR})$; m is an integer; $\Delta\nu \equiv \nu - \nu_0$ is the frequency detuning from the resonance frequency at ν_0 ; $FSR = \frac{c}{n_{\text{eff}}L}$ is the free spectral range; $a \equiv \exp(-0.5\alpha L)$; α being the power loss coefficient; L being the perimeter of each ring; n_{eff} is the effective index of the ring and r_0 is the reflection coefficient of the coupler.

For instance, Figure 2.2a and 2.2b shows the normalized transmission and group delay respectively of a micro-ring resonator consisting of typical photonic wire waveguide ($W = 450$ nm, $H = 250$ nm) in SOI, with ring radius $25 \mu\text{m}$, $r_0 = 0.995$, $\alpha = 3$ db/cm. Single micro-ring resonator operating in APF configuration is not suitable for DWDM applications as seen from Figure 2.2b due to its extremely narrow linewidth. CROWs on the other hand are ideal candidates to provide tunable maximally flat delay over a finite

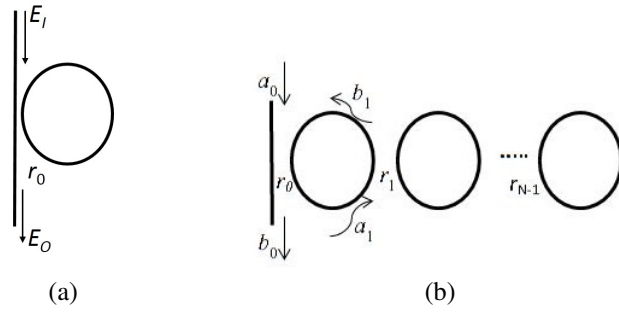


Figure 2.1: (a) Scheme of a single ring resonator operating in all-pass-filter configuration, (b) Schematic of a reflecting CROW with N identical ring resonators; a_n and b_n are incident and reflected field amplitude and r_n is the reflection coefficient at n^{th} designated coupler.

bandwidth for routing, buffering, synchronizing, multiplexing applications [52, 50].

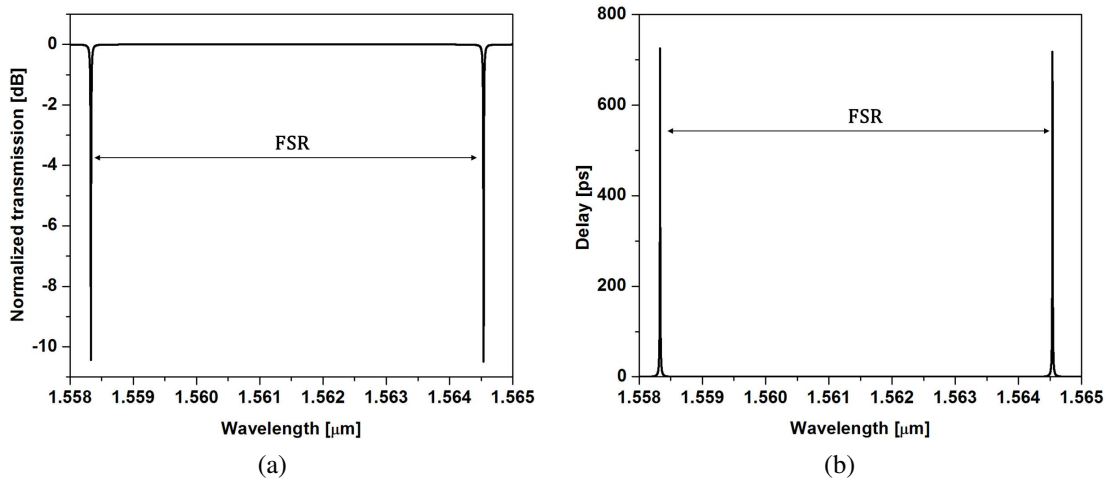


Figure 2.2: (a) Normalized transmission of micro ring resonator with a typical photonic wire waveguide ($W=450$ nm, $H=250$ nm) in SOI, with ring radius $25 \mu\text{m}$, $r_0 = 0.995$, $\alpha = 3$ db/cm (b) Corresponding group delay versus wavelength.

The N coupled rings in reflecting CROW configuration is shown in Figure 2.1b, in which a_n and b_n are incident and reflected field amplitudes, and r_n is the reflection coefficient at n^{th} designated coupler. To obtain a closed form transfer function of a

reflecting CROW, we first derive the transfer function of two-ring buffer as:

$$\frac{b_0}{a_0} = \frac{r_0 - \frac{r_1 - ae^{i\phi}}{1 - r_1 ae^{i\phi}} ae^{i\phi}}{1 - r_0 \frac{r_1 - ae^{i\phi}}{1 - r_1 ae^{i\phi}} ae^{i\phi}} = \frac{r_0 - f_1(r_1, ae^{i\phi}) ae^{i\phi}}{1 - r_0 f_1(r_1, ae^{i\phi}) ae^{i\phi}} \quad (2.2)$$

where $f_1 = \frac{b_1}{a_1}$ is the loading effect of second ring on the first ring. Therefore, one can continue to write transfer function for N coupled rings and simplify the resultant transfer function of first ring with loading factor f_{N-1} due to remaining N-1 rings. Thus the transfer function of the CROW structure can be formulated as:

$$\frac{b_0}{a_0} = \frac{r_0 - f_{N-1}(r_1, r_2, \dots, r_{N-1}, ae^{i\phi}) ae^{i\phi}}{1 - r_0 f_{N-1}(r_1, r_2, \dots, r_{N-1}, ae^{i\phi}) ae^{i\phi}} \quad (2.3)$$

As filter has a periodic frequency dependence in ϕ , we represent Eqn. (2.3) in Z-transform by replacing $exp(i\phi)$ with z^{-1} [54]. For small rings and low propagation loss one can assume $a \approx 1$ and get

$$A_N(z) = \frac{b_0}{a_0} = \frac{r_0 - f_{N-1}(r_1, r_2, \dots, r_{N-1}, z) z^{-1}}{1 - r_0 f_{N-1}(r_1, r_2, \dots, r_{N-1}, z) z^{-1}} \quad (2.4)$$

To extract the reflection (coupling) coefficients r_n ($\kappa_n = \sqrt{1 - r_n^2}$) we borrow concept from all-pass maximally flat filters [55, 56]. These filters give a flat delay for a finite bandwidth. Considering an N^{th} order all-pass-filter system, the response function can be written as:

$$T_N(s) = \frac{B_N(-s)}{B_N(s)} \quad (2.5)$$

where $B_N(s)$ is a Bessel's polynomial of order N for delay D satisfying the following recursive relations $B_N = (2N - 1)B_{N-1} + D^2 s^2 B_{N-2}$; $B_0 = 1$; $B_1 = Ds + 1$. Using bilinear transformation [54], one can obtain maximally flat all pass equivalent filter

response in Z-domain [57]:

$$T_N(z) = z^{-N} \frac{B_N(z^{-1})}{B_N(z)} \quad (2.6)$$

Comparing the coefficients of Eqn.(2.4) with Eqn.(2.6), we solve N linear equations to extract all the coupling coefficients - the values are in descending order.

2.1.2 Maximally Flat 8-bit Delay-Line in SOI

With the methodology discussed above, an 8 bit maximally flat delay line for DWDM applications (FSR = 200 GHz) using different order CROWs in SOI platform is designed. CROWs consisting of racetrack resonators with ring radius of 97 μm and straight coupling section of 10 μm is designed with single mode photonic wire waveguide (Width = 0.45 μm , Height = 0.25 μm). A standard 25 Gbps modulation is assumed. Optimized inter-ring coupling coefficients κ_N for 2nd, 4th, 6th, 8th order CROW for 8 bit maximally flat delay response is shown in Figure 2.3a. Using symmetric and anti-symmetric modes in a directional coupler, one can estimate the beat length for a given spacing (S). (see inset of Figure 2.3b) . Lumerical Mode Solutions was used to calculate the effective index of symmetric and anti-symmetric mode of this coupled system for TE polarization. Denoting $n_{\text{eff,sym}}$ and $n_{\text{eff,asym}}$ as the effective indices of symmetric and anti-symmetric modes, one can write for beat length L_b

$$\frac{2\pi}{\lambda} (n_{\text{eff,sym}} - n_{\text{eff,asym}}) L_b = \pi \quad (2.7)$$

One can have a relation between κ and S using

$$\kappa = \sin\left(\frac{\pi L_c}{2L_b}\right) \quad (2.8)$$

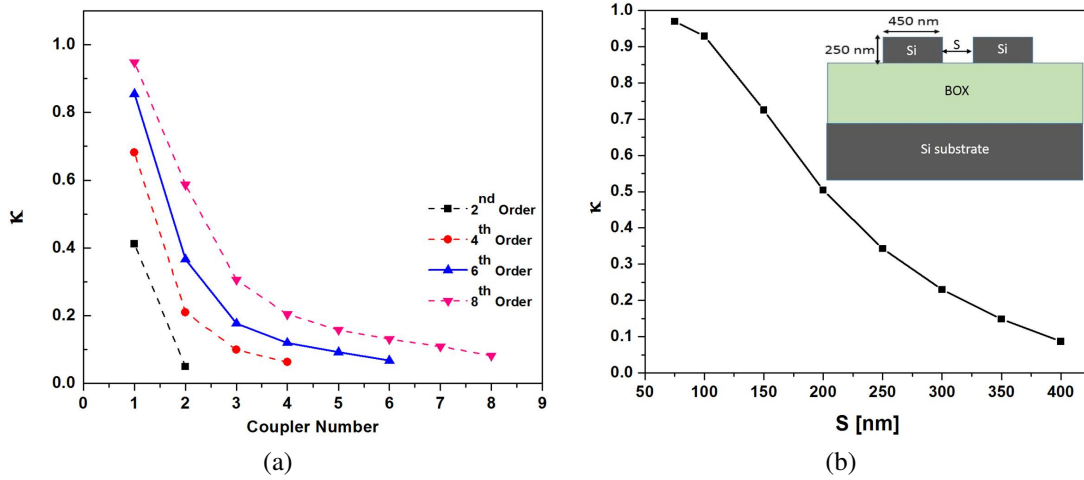


Figure 2.3: (a) Optimized inter-ring coupling coefficients for 2nd, 4th, 6th, 8th order CROWs for 8 bit maximally flat delay response. (b) Relation between coupling coefficient κ and spacing S for coupling length $L_c = 10 \mu\text{m}$ for the directional coupler consisting of photonic wire waveguides as shown in inset.

Where L_c is coupling length, which is shown in Figure 2.3b. Figure 2.4a shows the

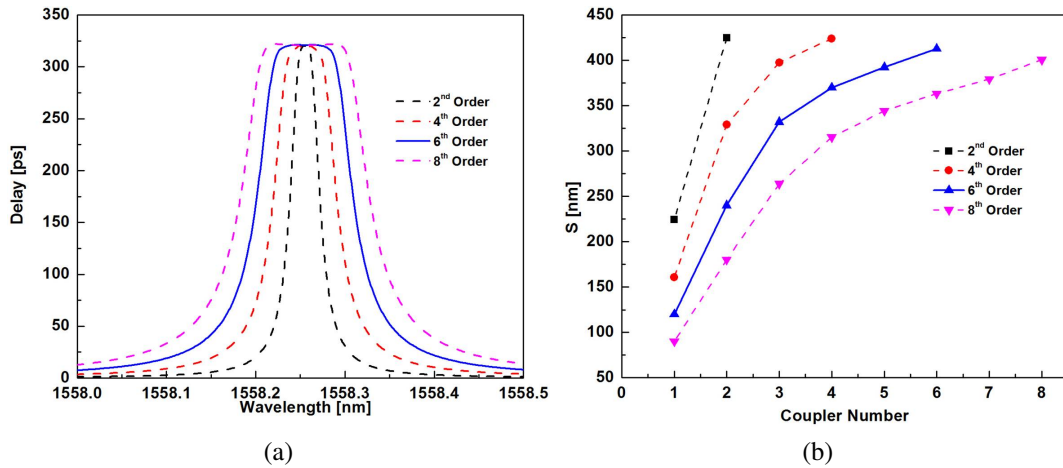


Figure 2.4: (a) Group delay vs wavelength (around a DWDM channel) for different order CROWs; (b) Extracted optimized separations between coupled waveguides shown in ascending order separately for 2nd, 4th, 6th, 8th order CROWs.

delay response as a function of wavelength for 2^{nd} , 4^{th} , 6^{th} and 8^{th} order CROWs. Figure 2.4b shows required coupler spacings for 2^{nd} , 4^{th} , 6^{th} and 8^{th} order CROWs. It is clearly observed from Figures 2.4a that for the same delay, higher order CROWs offer higher bandwidth. But, minimum separation needed for an 8^{th} order CROW as seen in Figure 2.4b is estimated to be ~ 30 nm which is difficult to achieve lithographically. It is seen that delay bandwidth product of reflecting CROW is $\sim 0.5N$, where N is the order of CROW. We take 6^{th} order CROW to be the optimal configuration for this scheme as it is easier to define coupler spacings of 50 nm, 160 nm, 250 nm, 290 nm, 320 nm and 355 nm respectively. Final schematic of sixth order CROW with optimized inter ring coupling coefficients and corresponding coupler spacings is shown in Figure 2.5a and 2.5b respectively. Here, C_i denotes the i^{th} coupler. It has been estimated that for a waveguide propagation loss of 0.5 dB/cm [58], the overall insertion loss for the above mentioned six-ring configuration is ~ 0.5 dB (assuming lossless couplers).

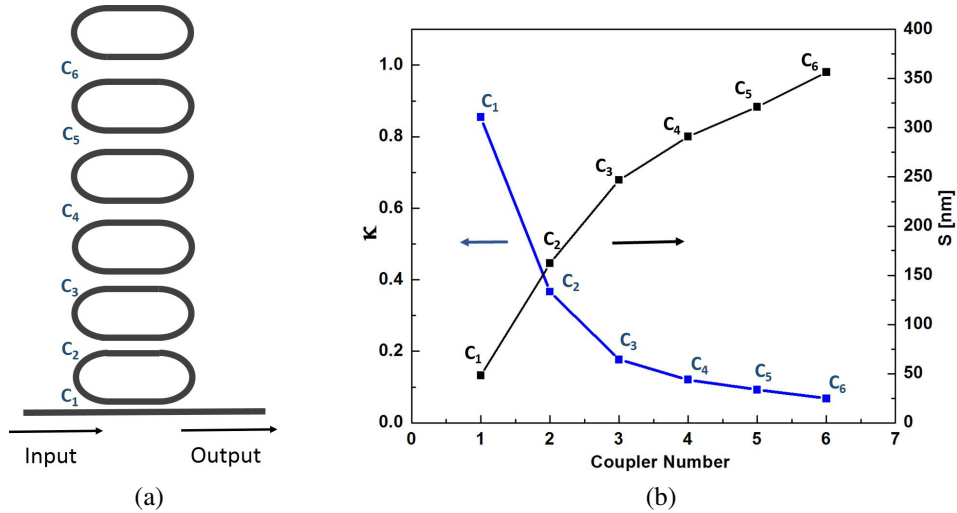


Figure 2.5: (a) Schematic of six CROW structure with ring radius of $97 \mu m$ and straight coupling section of $10 \mu m$ [denoted by $C_1, C_2 \dots C_6$]; (b) Cross-section of directional coupler with spacing S between single mode photonic wire waveguides. (c) Six coupling coefficients and corresponding spacing between coupled waveguides (apodized in ascending order) of 6^{th} order maximally flat CROW based delay line.

2.2 Fabrication Induced Disorder and Thermo-optic Compensation

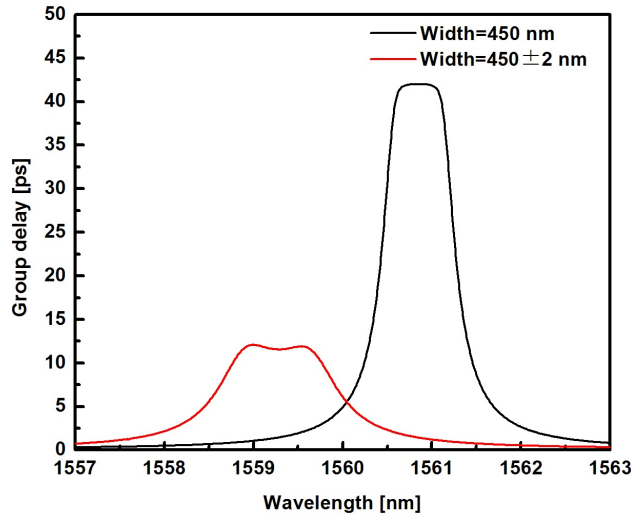


Figure 2.6: Fabrication induced disorder in 6th order maximally flat delay line: Black trace shows the ideal response when there is no fabrication imperfection across the ring resonators, red trace shows the degraded response when a probabilistic variation of 2 nm in waveguide width is considered across all the ring resonators.

Fabrication imperfections induced disorder in a sixth order maximally flat delay line is studied. Six racetrack resonators are identical having ring radius of 10 μm and a straight section of 10 μm . Photonic wire waveguide with $W = 450$ nm and $H = 250$ nm is considered. With the methodology discussed in previous section, coupling coefficients are extracted and a maximally flat delay response is achieved (black trace in Figure 2.6). To study fabrication intolerance, waveguide width is probabilistically varied across the six resonators and it is observed that a variation of 2 nm in waveguide width leads to a deleterious response (red trace in Figure 2.6).

This effect can be further analyzed if we plot effective index (n_{eff}) variation as a function of waveguide width W for different slab height h for TE polarization (see Figure

2.7b). A typical SOI rib waveguide geometry (see Figure 2.7a) with slab height (h), waveguide width (W) and rib height ($H = 250$ nm) with cladding 2 as air is considered. As observed from the figure n_{eff} variation is more for smaller slab heights. Due to this dependence, phase error accumulated for 1 nm of width variation for a length of 1 mm is nearly 2π radians at $\lambda = 1550$ nm. This poses a serious problem for multiplexing,

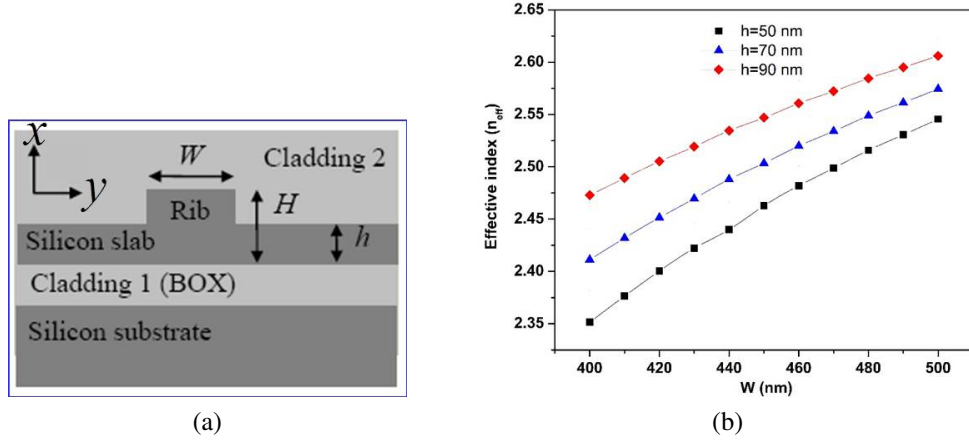


Figure 2.7: (a) Schematic of cross section of rib waveguide in SOI where H is rib height, h is slab height, W is width of waveguide. (b) Plot shows the dependence of n_{eff} on W for different h for a photonic wire rib waveguide of $H = 250$ nm.

routing applications based on devices viz. AWGs, coupled rings, MZIs etc. Nevertheless, high thermal sensitivity of silicon ($\frac{dn_{\text{eff}}}{dT} \sim 1.86 \times 10^{-4} K^{-1}$) ensures slight change in rib temperature locally can account for the phase error due to linewidth variation. It is seen that a temperature change of only 8 degrees is needed to change the phase by 2π radians at $\lambda = 1550$ nm for the same length of 1 mm.

It is to be noted that the case study of maximally flat delay lines using CROWs assumes ideal couplers with optimized coupling coefficients. Fabrication imperfections in definition of inter-ring spacings also leads to disorder in response. Thermo-optic phase shifters can be used to tune the inter ring coupling coefficients in CROWs thus correcting the phase error caused due to fabrication imperfections in gap definition between

successive rings.

Exploiting large thermo optic coefficient of silicon, Orlandi et al demonstrated in [59] variable power splitting using a directional coupler as shown in Figure 2.8. By

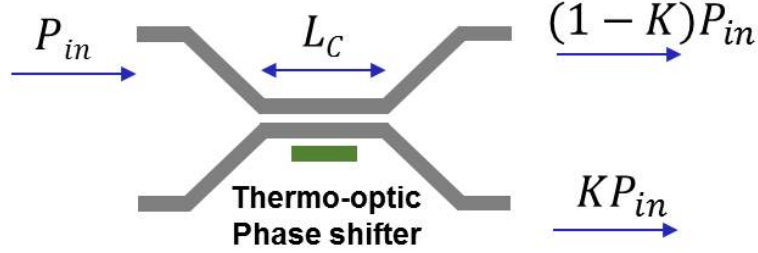


Figure 2.8: Variable power splitter driven by a transverse temperature gradient [59].

applying bias on thermo optic phase shifter, a transverse temperature gradient is created between two arms of directional coupler of length L_C , resulting in net phase mismatch $\Delta\beta$; Coupled power K is given by

$$K = \frac{|\kappa|^2}{S^2} \sin^2(SL_C) \quad (2.9)$$

where $S = (|\kappa|^2 + \Delta\beta^2/4)^{0.5}$, κ is field coupling coefficient; $\Delta\beta = 2\pi\Delta n/\lambda$.

2.3 Reconfigurable Delay lines

Reconfigurable CROW based delay lines were demonstrated by Morichetti et al [34]. Microheaters were deposited on successive ring resonators in series coupled configuration as seen in Figure 2.9a to achieve continuously tunable error free operation at 10 Gbit/s. Initially, all the rings are out of resonance to the input signal, by applying bias on successive phase shifters, ring resonators are brought into resonance by a tuning control unit as seen in Figure 2.9b and hence delay the input signal accordingly. Thus a contin-

uous tunable delay operation is achieved (Figure 2.9c).

But, successive phase shifters will lead to thermal crosstalk between rings. Thermal cross-talk remains a major bottleneck in large scale integration. This study gives us motivation to design a microheater in SOI platform with low switching power (P_π) and faster response time (τ). Moreover, it strives to understand the temperature distribution along the waveguide and effective heating zone due to applied bias on the microheater.

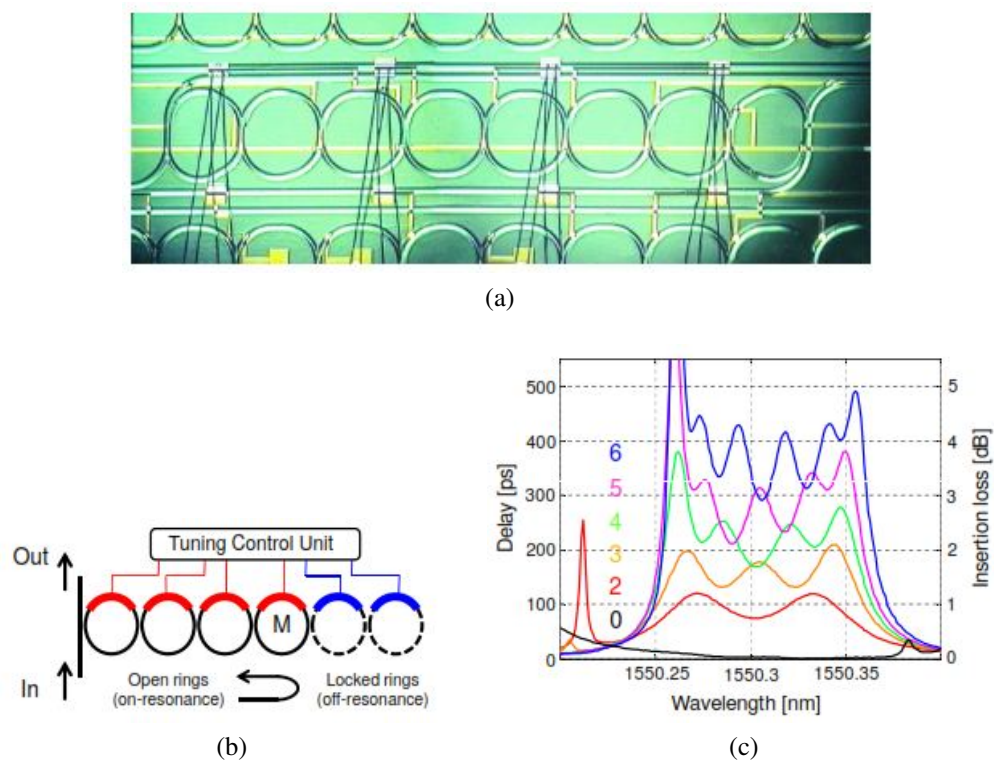


Figure 2.9: (a) Micrograph of series coupled microring resonators integrated with microheaters for tunable delay. (b) Mechanism of tuning of delay by selectively turning on ring resonators using microheaters based phase shifters. (c) Measured group delay and insertion loss for increasing number of rings in resonance [34].

2.4 Conclusions

A case study of maximally flat delay lines in SOI is presented. Phase error incurred due to fabrication imperfections leads to deleterious response. Microheaters based phase shifters can be employed to locally tune the phase error. Variable power splitters are specifically useful to tune the coupling coefficient in large scale circuits such as delay lines where error in spacing between ring resonators can lead to garbled response. Microheaters are useful to provide reconfigurable operation in delay line circuits. Thus, it is important to design an efficient microheater ; to understand its effective heating zone - thus enabling circuit designers to design complex reconfigurable circuits with lower thermal crosstalk.

CHAPTER 3

AN INTEGRATED OPTICAL MICROHEATER : THEORETICAL STUDY

This chapter begins with description of the design of slab deposited integrated optical microheaters adopted in this work. A detailed study of temperature distribution along the waveguide due to applied bias in slab deposited microheater is presented. A linear piece wise model to ascertain thermal distribution for both micron and sub micron cross section waveguides is also formulated. The chapter sums up with the transient analysis of microheaters using COMSOL based FEM simulations.

3.1 Design and Modelling

The Joule heating of a metallic microheater controls the effective refractive index (n_{eff}) of waveguide via thermo-optic effect. In general, thermo-optic switches are fabricated with over-clad microheaters [24, 39]. Thus the metallic microheaters remain optically insulated from the core region of the waveguides, but that advantage comes at the cost of relatively higher response time (τ_{resp}). Alternatively, metallic heaters are defined directly in the slab region of a rib waveguide but at a safe lateral distance from the core guiding region [41, 38], which in fact ensures faster response time. However, "thermal cross-talk" is a cause of concern in case of slab deposited microheaters; especially, for large-scale integrated circuits [36, 60]. Therefore, a working empirical model for the temperature profile of a typical slab deposited microheater has been developed which

eventually will help to assess its impact (or thermal cross-talk) on neighboring device performances.

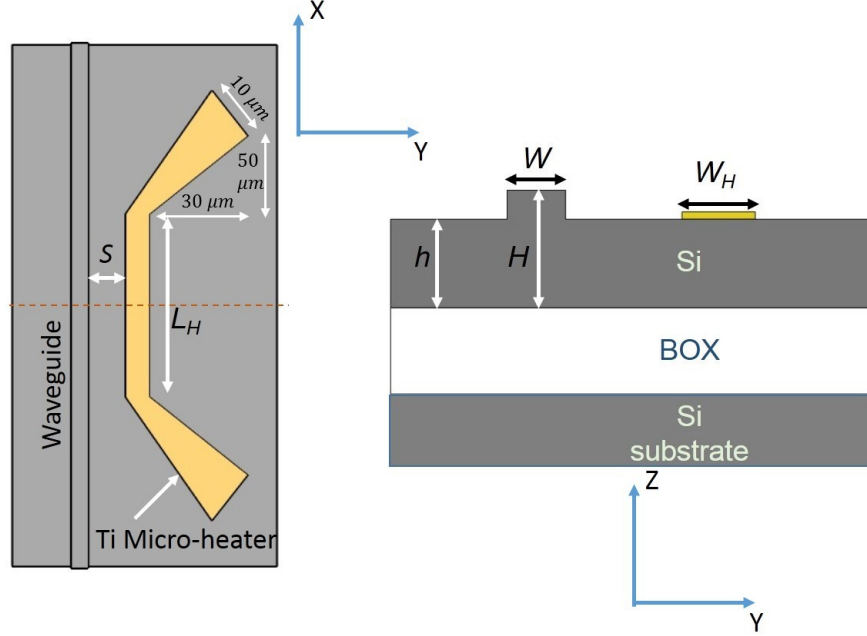


Figure 3.1: Top and cross-section views of a simple microheater design integrated with a single-mode SOI rib waveguide (width W , rib height H , slab height h). L_H and W_H are the heater length and width, respectively.

A simple design of a Ti-stripe microheater integrated in the slab region of single-mode rib waveguide and aligned parallel to the guiding axis has been considered for our study. Slab deposited microheaters integrated with rib waveguides facilitates easier characterization of microheater performance using simple characterization setup. Here Ti is preferred as the heating element because of its high resistivity, high melting point and CMOS compatibility. Figure 3.1 shows the scheme of such a microheater along with a rib waveguide in SOI platform. Depending on the SOI device layer thickness H , one can find a suitable waveguide width W and slab thickness h for well-confined single-mode guidance for a given operating wavelength λ [61]. The microheater has a central heating zone of length L_H with narrow stripe of width W_H and thickness t_H ; and

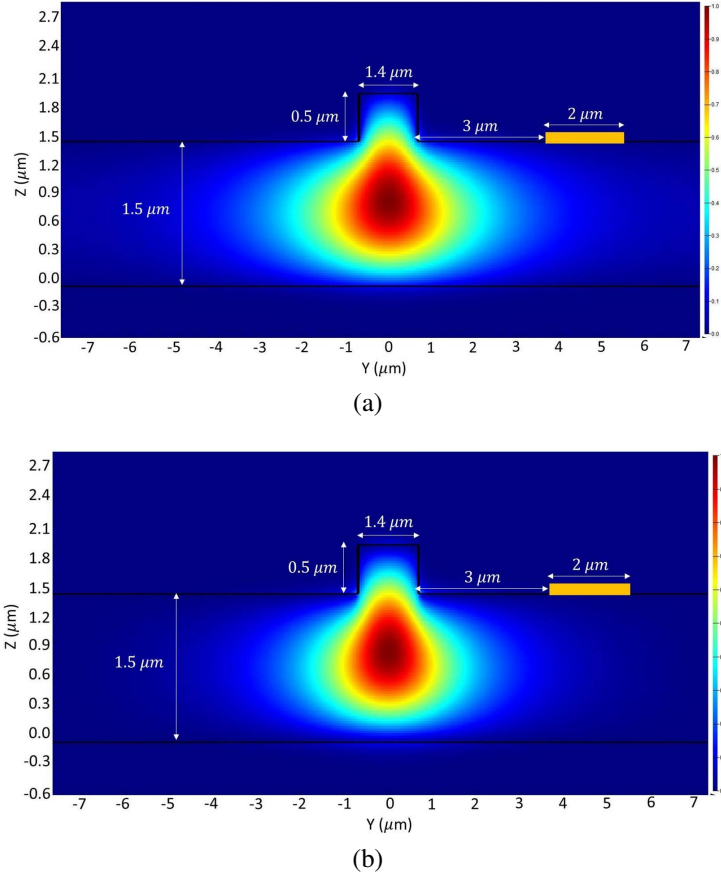


Figure 3.2: Calculated electric field profiles for a single-mode SOI rib waveguide with $H = 2 \mu\text{m}$, $W = 1.4 \mu\text{m}$ and $h = 1.5 \mu\text{m}$: (a) E_y component for TE-polarization, and (b) E_z component for TM polarization. The microheater shown in yellow-strip is kept at a separation of $3 \mu\text{m}$ from rib edge to avoid overlap with the guided fields.

flaring terminals of width $5W_H$ to ensure lower power dissipation towards terminal contact pads. The thickness of the heater (t_H) is another important parameter to define the resistance per unit length. A minimum separation of S is required between waveguide and heater to avoid unwanted metal overlap with the guided mode causing polarization dependent attenuation [62]. Calculated electric field distributions for TE-mode (E_y component) and TM-mode (E_z component) for a given single-mode waveguide geometry ($H = 2 \mu\text{m}$, $W = 1.4 \mu\text{m}$ and $h = 1.5 \mu\text{m}$) are shown in Figure 3.2. The metallic

microheater (shown in yellow color) is kept at $3 \mu\text{m}$ away from rib edge for both micron and sub micron waveguides. This is to ensure metal overlap with the guided mode is negligible. It must be noted that the heater position can be even closer to the ridge edge to ensure lower metallic-loss and better thermo-optic overlap, if the single-mode waveguide is design with tighter modal confinements. If we ignore the edge-effect and assume

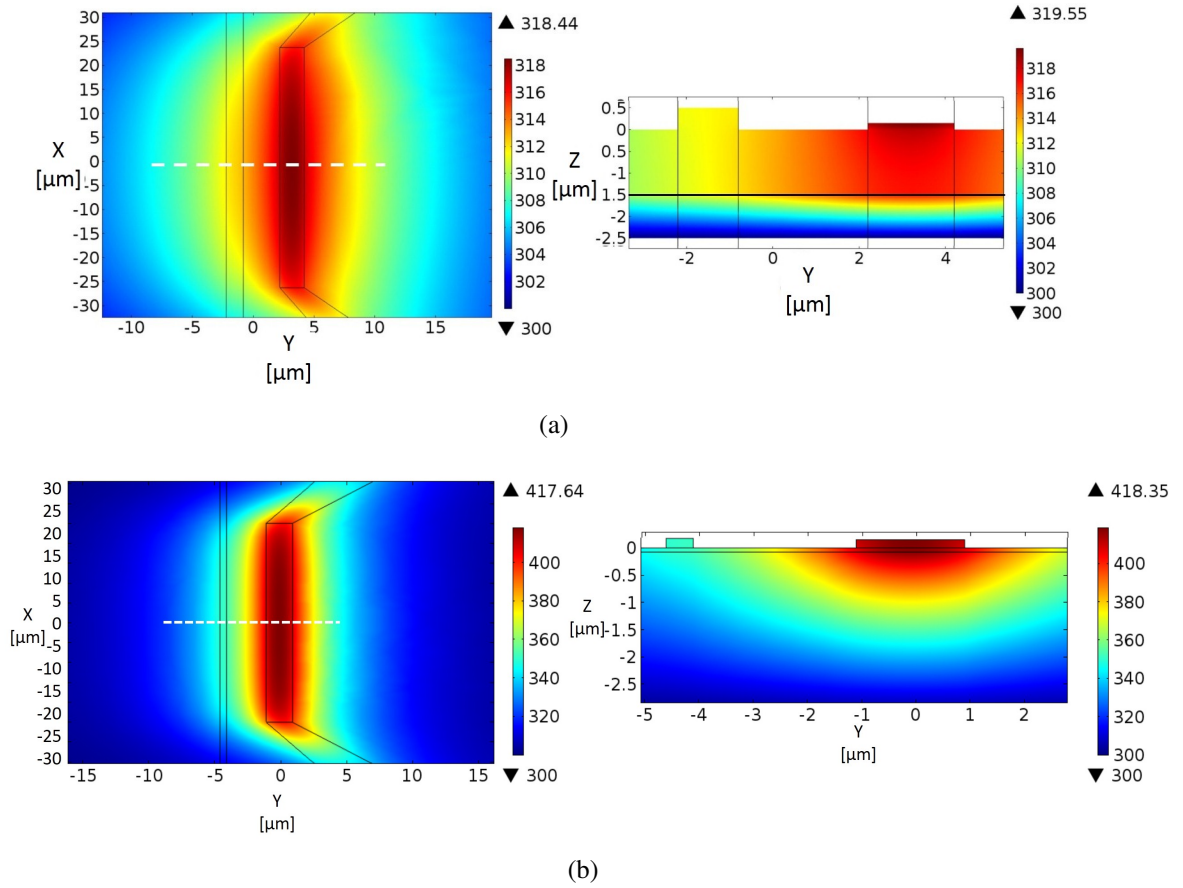


Figure 3.3: Simulated top and cross-section (across the dotted line) temperature profile of the microheater (Ti stripe with $W_H = 2 \mu\text{m}$, $L_H = 50 \mu\text{m}$, $t_H = 150 \text{ nm}$, $S = 3 \mu\text{m}$): (a) Integrated with rib waveguide ($W = 1.4 \mu\text{m}$, $H = 2 \mu\text{m}$, $h = 1.5 \mu\text{m}$) for an applied bias of $i_H = 0.9 \text{ mA}$. (b) Integrated with rib waveguide ($W=500 \text{ nm}$, $H= 250 \text{ nm}$, $h = 0.075 \text{ nm}$) for an applied bias of $i_H = 0.9 \text{ mA}$.

uniform heating along the waveguide of length L_H (same as the length of microheater),

the change in phase $\Delta\phi$ of the guided mode due to thermo-optic effect is given by:

$$\Delta\phi = \frac{2\pi}{\lambda} \Delta n_{\text{eff}} \cdot L_H \simeq \frac{2\pi}{\lambda} \left(\frac{dn_{\text{Si}}}{dT} \right) \Delta T \cdot L_H \quad (3.1)$$

Where Δn_{eff} is change in effective index due to change in temperature ΔT . In this equations, we have assumed $\frac{dn_{\text{eff}}}{dT} \approx \frac{dn_{\text{Si}}}{dT}$, as it is evident from our theoretical simulations using Lumerical mode solver. However, FEM simulation shows that the temperature distribution along the waveguide is far from uniform. The edge-effect is significant; especially, for shorter heater length.

Figure 3.3 a,b shows the temperature distributions exactly on the slab surface (heater plane) and cross-sectional plane of a single-mode waveguide with $H = 2 \mu\text{m}$, $W = 1.4 \mu\text{m}$ and $h = 1.5 \mu\text{m}$ and sub micron waveguide with $W = 500 \text{ nm}$, $H = 250 \text{ nm}$, $h = 0.075 \mu\text{m}$ respectively ; for $L_H = 50 \mu\text{m}$, $W_H = 2 \mu\text{m}$, $t_H = 150 \text{ nm}$, $S = 3 \mu\text{m}$ and for an applied current $i_H = 0.9 \text{ mA}$ between the microheater terminals. The 2D temperature profiles have been extracted by 3D FEM calculations using Joule heating module of Comsol Multiphysics simulator. It is evident from the XY temperature profile in figure 3.3 a,b that effective heating zone for micron cross section waveguide is larger compared to sub micron cross section waveguide. This effect is further reflected and explained in the piecewise model developed in the next section. Moreover, the peak temperature for same bias is also higher in sub micron waveguide compared to micron cross section waveguide. Smaller effective heating zone ensure heat loss to surroundings is minimized in sub micron waveguides. The temperature profiles shown in Figure 3.3 a,b is a zoomed region of interest - the actual simulation window was 120- μm -wide, 300- μm -long, and 3- μm -deep (assuming air above the top surface and 1 μm BOX/SiO₂ below the device layer), with convective boundary condition at top surface and thermal insulation at the lateral boundaries, whereas constant room temperature at bottom edge.

It is evident from the cross-sectional profile (in y-z plane) that the core region of

the waveguide has a little temperature gradient. However, there is a wide range of temperature distribution observed along the waveguide (x-axis). The differential change in temperature (δT) along the micron waveguide ($W = 1.4 \mu\text{m}$, $H = 2 \mu\text{m}$, $h = 1.5 \mu\text{m}$) has been shown in Figure 3.4a for four different values of applied current $i_H = 0.9 \text{ mA}$, 1.5 mA , 2.1 mA , 2.7 mA .

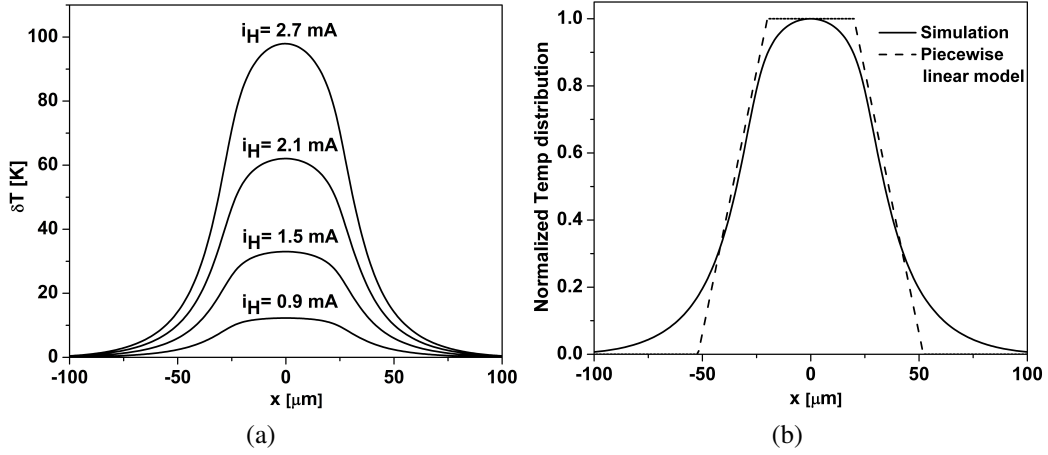


Figure 3.4: (a) Temperature distributions along the waveguide for $L_H = 50 \mu\text{m}$, for different applied current i_H for ($W = 1.4 \mu\text{m}$, $H = 2 \mu\text{m}$, $h = 1.5 \mu\text{m}$). (b) Normalized temperature distribution and piecewise linear model plotted as a function of distance along the waveguide.

As expected, the change in temperature peaks at the center and remain non-zero even at a large distance from the heater edge. Interestingly, the actual temperature profile (for a given applied current i_H) can be derived from a characteristic normalized distribution function $f(x)$ after multiplying the peak temperature change $\delta T_p(i_H)$. Therefore, Eqn. (3.1) needs to be modified as:

$$\Delta\phi \simeq \frac{2\pi}{\lambda} \left(\frac{dn_{\text{Si}}}{dT} \right) \delta T_p(i_H) \int f(x) dx \quad (3.2)$$

Integrating $f(x)$ along the length of waveguide gives the "effective length" of the heater:

$$L_{\text{eff}} = \int f(x)dx \quad (3.3)$$

A piecewise linear model has been formulated to fit this normalized distribution function and shown pictorially in Figure 3.4b. Since the distribution function is symmetrical around the origin at $x = 0$, it is sufficient to model only half of the function ($x \geq 0$) for a given heater of length $L_H = 2L_0$:

$$f(x) = g(x)H[g(x)] \quad (3.4)$$

where $H[g(x)]$ is the Heaviside step function and $g(x)$ is given by:

$$\begin{aligned} g(x) &= 1 & \forall 0 \leq x < L_0 - \alpha \\ &= 1 - m[x - (L_0 - \alpha)] & \forall x \geq L_0 - \alpha \end{aligned} \quad (3.5)$$

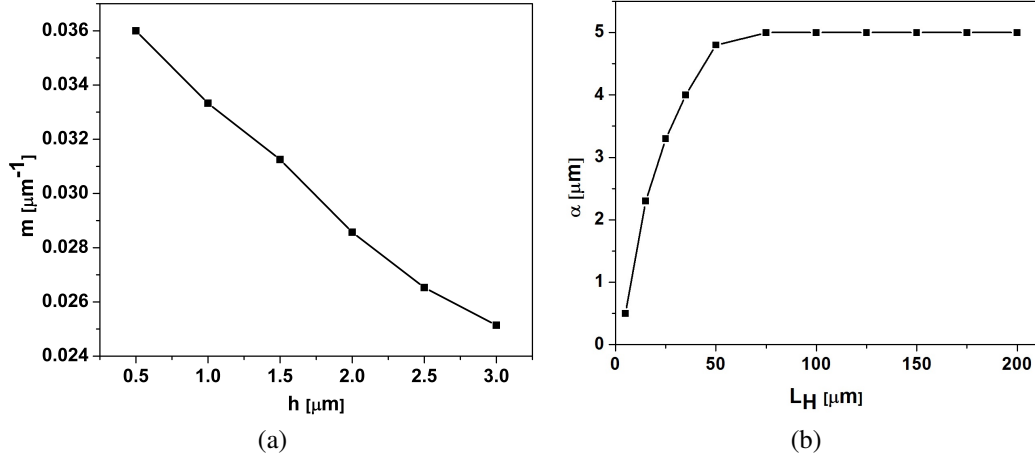


Figure 3.5: (a) Dependence of slope m on slab height h . (b) Variation of offset α as a function of L_H .

In this model, we have used two fitting parameters; offset α and slope m to estimate

the edge-effect of a microheater. We observe that the value of m decreases with the increase of slab height h (see Figure 3.5a) and found to be independent of W_H and L_H . The value of offset α has been found to be nearly independent of slab height within the region of our interest ($500 \text{ nm} \leq h \leq 3 \text{ }\mu\text{m}$). α signifies the proportion of edge-effect which reduces and finally stabilizes with the increase of heater length as seen in Figure 3.5b.

Table 3.1: Calculated L_{eff} of a Ti thinfilm microheater design (as shown in Figure 3.1) values for different L_H for $W = 1.4 \text{ }\mu\text{m}$, $h = 1.5 \text{ }\mu\text{m}$, $H = 2 \text{ }\mu\text{m}$, $W_H = 2 \text{ }\mu\text{m}$, $S = 3 \text{ }\mu\text{m}$, $t_H = 150 \text{ nm}$

L_H [μm]	5	25	50	100	200
L_{eff} [μm]	36	49	73	122	222

Table 3.2: Calculated L_{eff} of a Ti thin film microheater design (as shown in Figure 3.1) values for different L_H for $W = 500 \text{ nm}$, $h = 75 \text{ nm}$, $H = 250 \text{ nm}$, $W_H = 2 \text{ }\mu\text{m}$, $S = 3 \text{ }\mu\text{m}$, $t_H = 150 \text{ nm}$

L_H [μm]	5	25	50	100	200
L_{eff} [μm]	29	38	63	112	212

By using the above model, one can estimate the effective heater length L_{eff} from Eqn. (3). Calculated L_{eff} values for different L_H have been shown in Table 3.1 and 3.2 for the single-mode waveguide design with a slab height of $h = 1.5 \text{ }\mu\text{m}$ ($W = 1.4 \text{ }\mu\text{m}$ and $H = 2 \text{ }\mu\text{m}$) and $h = 75 \text{ nm}$ ($W = 500 \text{ nm}$ and $H = 250 \text{ nm}$) respectively. For waveguides with thinner device layer thickness, the values of m is larger compared to waveguides with thicker device layer, which manifests itself in smaller L_{eff} for a given L_H . This is expected as effective thermal conductance through silicon increases with higher slab height. It is worth mentioning here that by the knowledge of change in phase of a guided mode, one can estimate the change in peak temperature (δT_p) in the waveguide using Eqns. (3.2) and (3.3). Subsequently, one can evaluate the length and/or geometry dependent figure of merit of a microheater.

3.2 Transient Analysis

Transient response of microheater is studied using time dependent study of Joule heating module in COMSOL *Multiphysics*TM for both micron ($H = 2 \mu\text{m}$, $W = 1.4 \mu\text{m}$ and $h = 1.5 \mu\text{m}$) and sub micron ($H = 250 \text{ nm}$, $W = 500 \text{ nm}$ and $h = 75 \text{ nm}$) cross section waveguide. A square voltage pulse $V_H(t)$ (50 % duty cycle and frequency 20 KHz) is applied on microheater terminals and average Temperature profile in waveguide is recorded as a function of time for W_H viz. $2 \mu\text{m}$ and L_H viz. $50 \mu\text{m}$, $100 \mu\text{m}$, $200 \mu\text{m}$ for both waveguide geometry. Amplitude of square pulse $V_H(t)$ is set such that peak temperature change in waveguide induces a round trip phase shift of π . Amplitude is 3 V for micron cross section waveguide and 1.3 V for sub micron cross section waveguide. Difference in bias values for micron and sub micron cross section waveguide can be

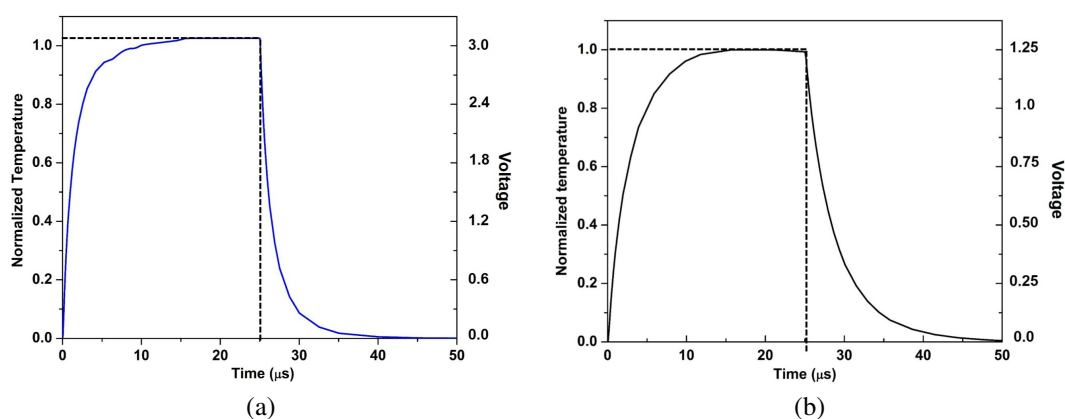


Figure 3.6: (a) Simulated transient response of micron cross section waveguide ($W = 1.4 \mu\text{m}$ and $h = 1.5 \mu\text{m}$) with Ti micro heater ($W_H = 2 \mu\text{m}$, $t_H = 150 \text{ nm}$, $L_H = 200 \mu\text{m}$); T_{rise} (T_{fall}) = $4.3 \mu\text{s}$ ($4.4 \mu\text{s}$). (b) Simulated transient response of sub micron cross section waveguide ($W = 500 \text{ nm}$ and $h = 75 \text{ nm}$) with Ti micro heater ($W_H = 2 \mu\text{m}$, $t_H = 150 \text{ nm}$, $L_H = 200 \mu\text{m}$); T_{rise} (T_{fall}) = $7.8 \mu\text{s}$ ($9 \mu\text{s}$). Black dotted trace shows the input square pulse ($V_H(t)$) with 50 % duty cycle and frequency 20 KHz.

explained from Figure 3.3 a,b. Effective heating zone of micron cross section waveguide is larger compared to sub micron cross section waveguide, thus electrical bias needed to

induce same peak temperature change is also higher. Figure 3.6 a,b shows the simulated transient response of micron and sub micron cross section waveguide respectively for $W_H = 2 \mu\text{m}$, $t_H = 150 \text{ nm}$, $L_H = 200 \mu\text{m}$. Y-axis shows the normalized temperature change in the waveguide for an applied square signal $V_H(t)$ on microheater terminals (black dotted trace). Typical T_{rise} (T_{fall}) of microheater for micron and sub micron cross section waveguide is calculated to be $\sim 4.3 \mu\text{s}$ ($4.4 \mu\text{s}$) and $7.8 \mu\text{s}$ ($9 \mu\text{s}$) respectively. This difference in response time can be understood if we look at Figure 3.7 a,b. Effective thermal conductance through silicon increases with slab height.

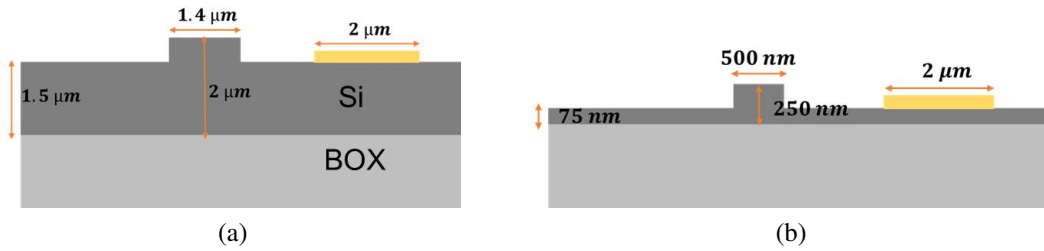


Figure 3.7: (a) Cross-section of $2 \mu\text{m}$ SOI ($W = 1.4 \mu\text{m}$ and $h = 1.5 \mu\text{m}$) with Ti micro heater ($W_H = 2 \mu\text{m}$, $t_H = 150 \text{ nm}$). (b) Cross-section of 250 nm SOI ($W = 500 \text{ nm}$ and $h = 75 \text{ nm}$) with Ti micro heater ($W_H = 2 \mu\text{m}$, $t_H = 150 \text{ nm}$).

Higher slab height in case of micron cross section helps in conducting heat faster from heater to waveguide compared to a 250 nm SOI where silicon slab height is only $\sim 75 \text{ nm}$. No appreciable variation is observed in response time for different microheater length L_H viz $50 \mu\text{m}$, $100 \mu\text{m}$, $200 \mu\text{m}$ for both geometries.

3.3 Conclusions

In this chapter, a simple design of slab deposited microheater is first discussed. A linear piecewise model for an integrated optical microheater is then presented. The model helps to calculate the effective heater length and the temperature distribution along the

waveguide. The model is equally valid for micron to submicron waveguide cross sections. It is observed that effective heater length has a dependence on slab height of waveguide. Finally, the chapter concludes with the transient analysis of the microheater.

CHAPTER 4

EXPERIMENTAL INVESTIGATIONS

This chapter begins with overview of design and fabrication of optical masks for microheaters. Optimized fabrication processes and parameters are discussed in detail next. Loss and mode profile measurement is discussed as well. The model developed in previous chapter has been used to evaluate the performance of the fabricated microheaters. Both static and transient response of microheaters is presented.

4.1 Mask Design for Device Fabrication

Fabrication process for microheaters integrated with rib waveguides involves three photolithography steps, hence three photo masks were fabricated. The first mask is used to define the rib waveguides, second for contact pads and third for definition of microheaters. The mask layouts were created using RAITH 150^{TWO} GDSII software. Combined Mask layout consisting of microheaters and probe pads integrated with rib waveguides is shown in Figure 4.1. First mask consisted of a total of 36 waveguides of $W = 1.4 \mu\text{m}$ and 20 mm long each separated by $250 \mu\text{m}$ (out of which 6 were reference waveguides and rest were integrated with microheaters) and a slab $50 \mu\text{m}$ wide. Second mask contained patterns for contact pads. Contact pads were $200 \mu\text{m} \times 250 \mu\text{m}$ in dimensions, to ensure sufficient area for probing. Final mask is a dark field mask with total of 15 microheaters each of $W_H = 2 \mu\text{m}$ and $3 \mu\text{m}$ respectively, for different $L_H = 50 \mu\text{m}, 100 \mu\text{m}, 200 \mu\text{m}$. Each mask had alignment marks for proper lateral and angular alignment. Slab waveguide facilitated easier coupling of light into the sample.

Schematic of mask layout is presented in Figure 4.2. Structures created by the software were transferred to the commercially procured PPR coated mask plate using DWL66 mask writer ($\lambda \sim 442$ nm). Patterned photoresist was developed using TMAH based standard developer (MicropositTM MF319) for 40 secs. Chromium etching was done next to remove unwanted Cr using Ortho-phosphoric acid based wet etchant for 90 secs. Finally remaining PPR was removed with boiling acetone and Piranha.

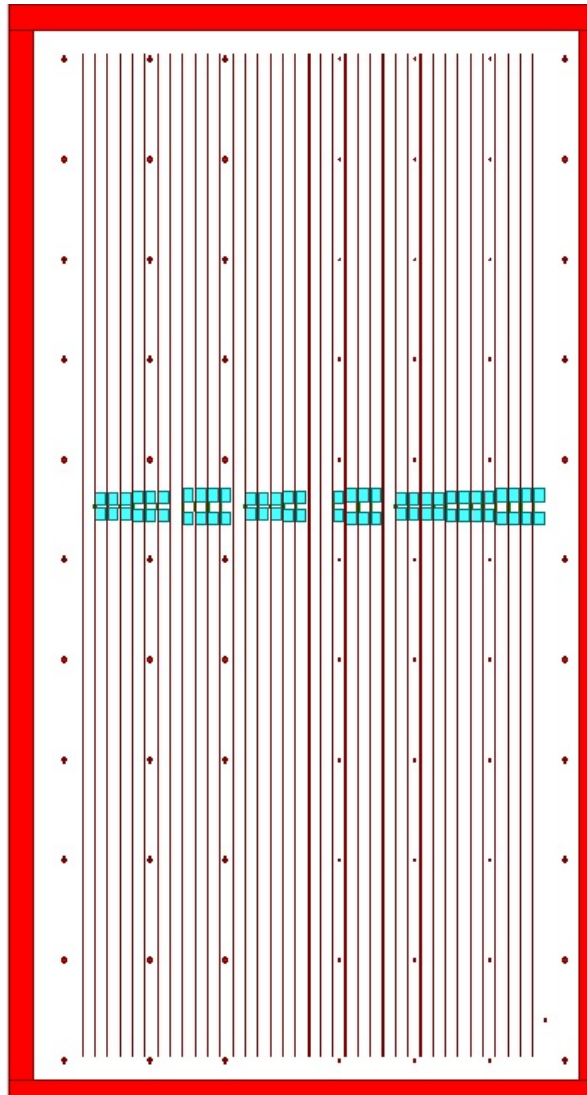


Figure 4.1: Combined mask layout of microheaters along with probe pads (blue) integrated with rib waveguides (red).

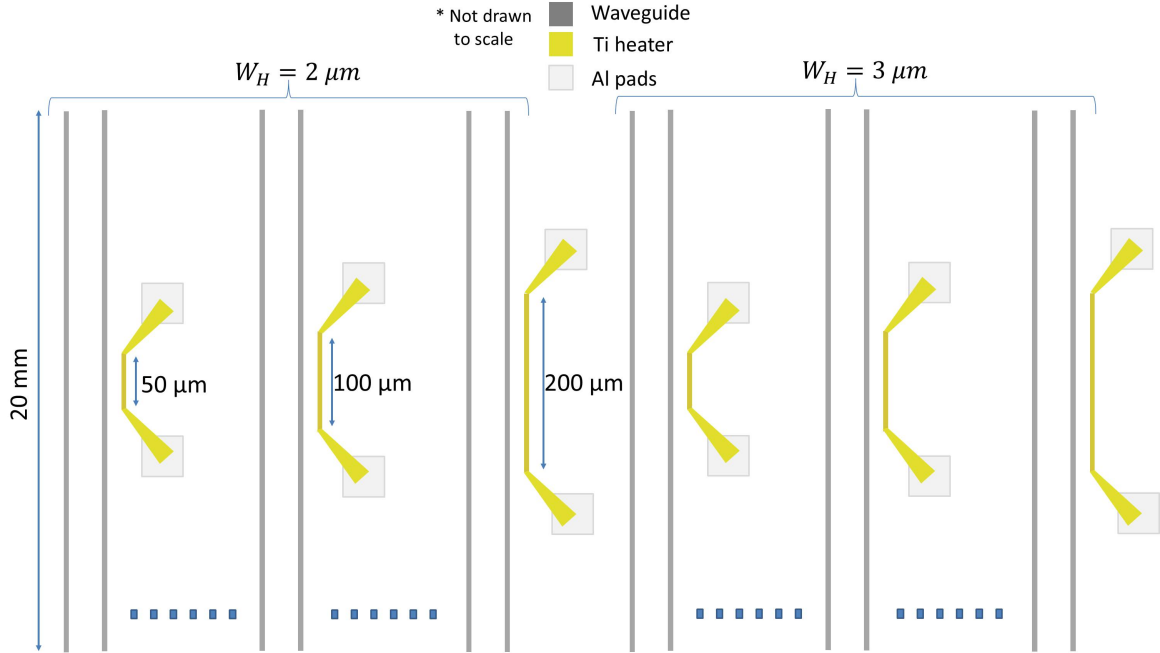


Figure 4.2: Schematic of mask layout of microheaters integrated with rib waveguides: A total of 36 waveguides (grey) were defined, out of which 6 were reference waveguides and rest were integrated with microheaters (yellow) and contact pads (white).

4.2 Device Fabrication

Process optimization was carried out in cheaper Silicon wafers before implementing the same on SOI wafers. The specification of SOI wafer is presented in Table 4.1. Device was fabricated in $2 \mu m$ SOI as it is easier to couple light into micron cross section waveguides with standard end fire characterization setup.

Table 4.1: SOI wafer specifications

Doping	P-type
Resistivity	$\sim 5 \text{ K}\Omega\text{-cm}$
Crystal Orientation	$\langle 100 \rangle$
Device layer thickness	$2 \mu m$
BOX layer thickness	$1 \mu m$
Handle Wafer thickness	$500 \mu m$

Fabrication process flow adopted for fabricating microheaters integrated with rib waveguides is shown in Figure 4.3. The critical step in this process flow is the definition of microheaters, hence it is the final step. Initially, sample was cleaned using TCE, ac-

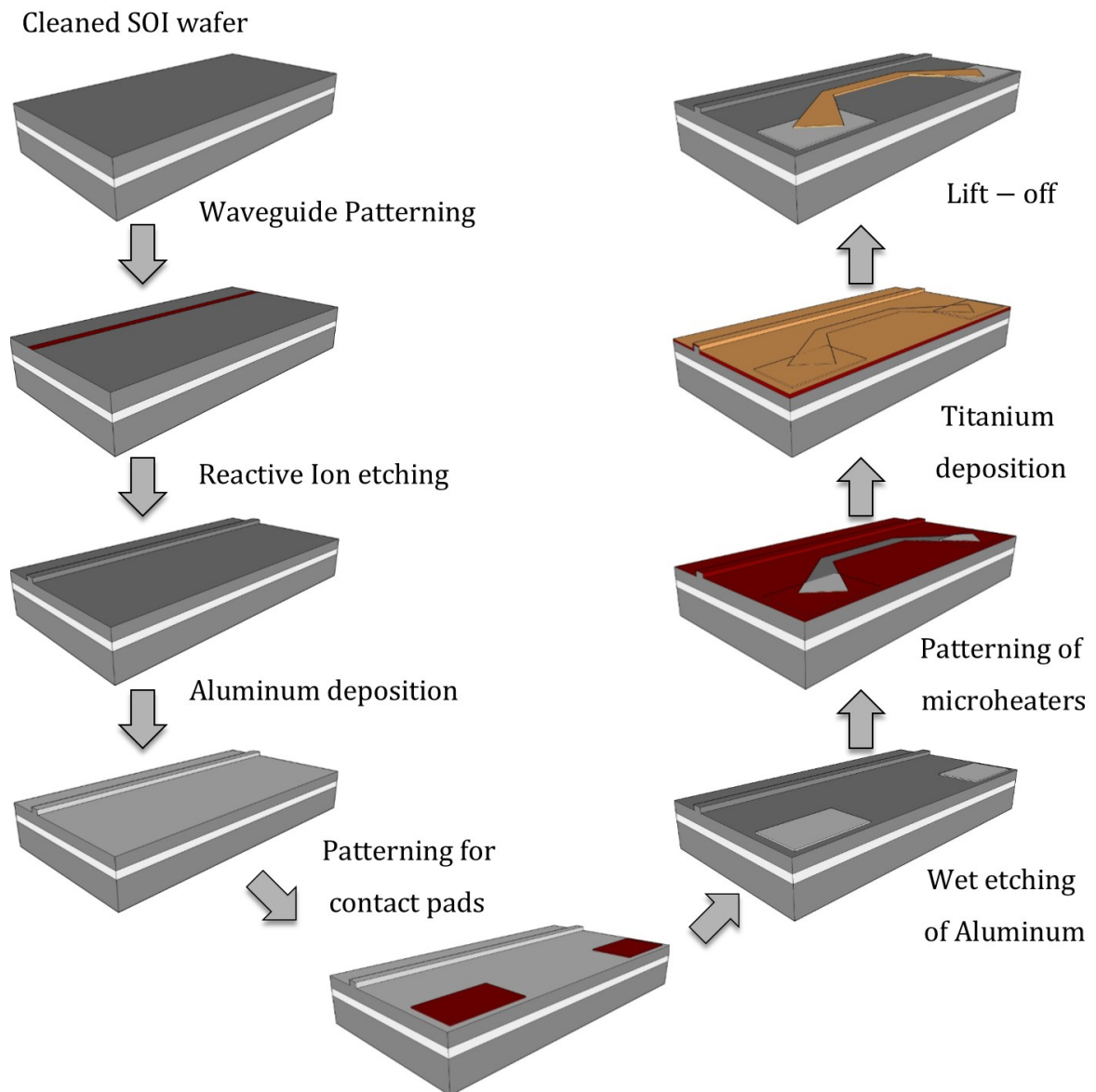


Figure 4.3: Fabrication process flow of microheaters integrated with rib waveguides.

tone, nitric acid and hydrofluoric acid. This was done to remove organic and inorganic

contaminants. PPR S1805 - MicropositTM was spin coated next with the optimized spin coating parameters: Speed 3000 rpm, Acceleration 450 rpm/s, Time 45 seconds, to get a thickness of ~ 500 nm. PPR was then hardened by prebaking the sample @ 120°C in a convective oven for 8 mins. This was done to remove excess solvent and to avoid sticking of PPR onto the mask plate while aligning. The sample was aligned with MA6/BA6 mask aligner using waveguide mask and exposed to i-line UV (lamp intensity ~ 15 mW/cm²) for 10 seconds. Next, PEB was done @ 80°C in a convective oven for 2 mins to remove line edge roughness in PPR sidewalls. Development of sample was carried out next using TMAH based standard developer MF321 for 45 seconds. Finally, Post-baking of sample was done for 20 mins @ 80°C to improve etching resistance of PPR. Patterns were subsequently transferred onto sample using Oxford Instruments PlasmaLab 80 reactive ion etching system. SF₆/Ar based chemistry is used to get smooth and vertical sidewalls [63]. With the optimized etching recipe (see Table 4.2), waveguides were etched for ~ 0.5 μ m. PPR mask was removed by ultrasonic agitation

Table 4.2: Optimized etching parameters.

Gas flow rate	SF ₆ :Ar::20:20 sccm
Pressure	200 mTorr
RF power	150 W
Table Temperature	20°C
DC Bias	38 V
Etch rate	~ 0.37 μ m/min

of sample in acetone for two mins. Patterning of probe pads was done next. First, thermal evaporation of Aluminum was done and Al thickness of ~ 300 nm was achieved. Then, PPR S1805 was spin-coated with the same coating parameters as described before. PPR was hardened for 8 mins @ 120°C. Sample was then aligned by alignment marks present on the sample and the mask using mask aligner. Sample was exposed for 10 seconds in UV lamp (i-line) and developed using MF321 for 20 seconds. Sample was post-baked for 10 minutes in 80°C convective oven. Ortho-phosphoric acid based wet

etchant was used to etch excess Al. Etch rate was ~ 100 nm/min @ 22°C . PPR mask was removed using ultrasonic agitation in acetone. Patterning of microheaters was done next. S1805 resist was used to define microheaters, with same optimized parameters as discussed above. Titanium of thickness ~ 150 nm was deposited using e-beam evaporation. Lift-off of the resist was done next to remove excess Titanium. But, as seen from Figure 4.4, Titanium gets deposited on the waveguides as well. This is due to non con-

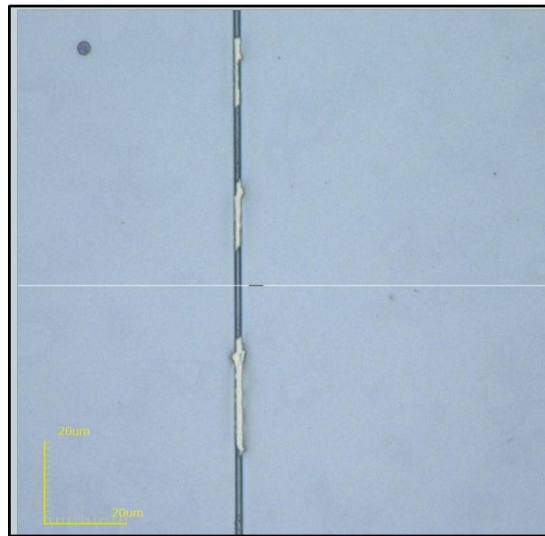


Figure 4.4: Confocal image showing Titanium remnants on waveguide due to non conformal coating of thinner resist S1805 on top of waveguide.

formal coating of thinner resist on top of waveguides. Instead, S1813-MicropositTM resist was used to define microheaters. S1813 is a thicker resist compared to S1805, which helps in conformal step coverage over waveguides. Resist was spin-coated with the optimized coating parameters: Speed 3000 rpm, Acceleration 500 rpm/s, Time 60 seconds, to get thickness ~ 1 μm . Sample was then pre-baked @ 80°C for 20 minutes. Mask aligner was used to align the sample with microheater mask with the help of alignment marks. Exposure was done for 12 seconds under UV lamp (i-line). PEB was done @ 80°C for 2 mins. Development of the exposed sample was carried out using standard developer MF321 for 35 seconds. Titanium of thickness ~ 150 nm was

deposited using e-beam evaporation. Lift-off of the resist was done next to remove excess Titanium. Initially, ultrasonic agitation was done in acetone to lift off excess metal and resist, but results were far from optimal as seen in Figure 4.5 where excess Ti got redeposited back onto the sample. To ensure excess metal doesn't stick to the sample, Ultrasonic agitation in Acetone, IPA, DI water was repeatedly done in separate beakers for two minutes each. Agitation in IPA ensured that PPR residue and metal remnants are removed. Finally DI water agitation cleans the sample completely. Figure 4.6a shows

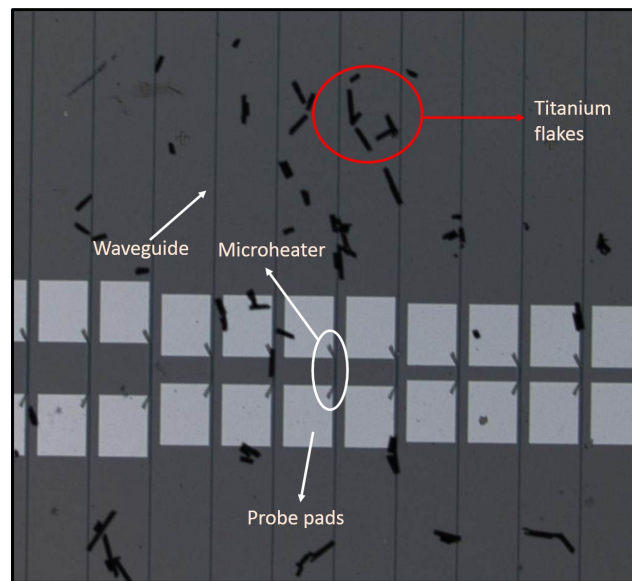


Figure 4.5: Confocal image of Ti microheaters integrated with waveguides after Titanium lift off, black spots (circled in red) correspond to Titanium flakes. Waveguide, microheaters and probe pads are labeled accordingly

the photograph of microheaters of different L_H viz. $50 \mu\text{m}$, $100 \mu\text{m}$ and $200 \mu\text{m}$. Black marks on Al pads are scratches incurred while probing. Figure 4.6b depicts the confocal micrograph of a microheater with $L_H = 100 \mu\text{m}$, $W_H = 2 \mu\text{m}$. Shown in the Figure are Al contact pads, waveguide and Ti microheater. End facets of the fabricated sample was polished with different polishing sheets of decreasing roughness starting from $30 \mu\text{m}$ to $0.5 \mu\text{m}$. This ensured optical quality end facets. SEM image of polished end-facet of a typical waveguide is shown in Figure 4.6c.

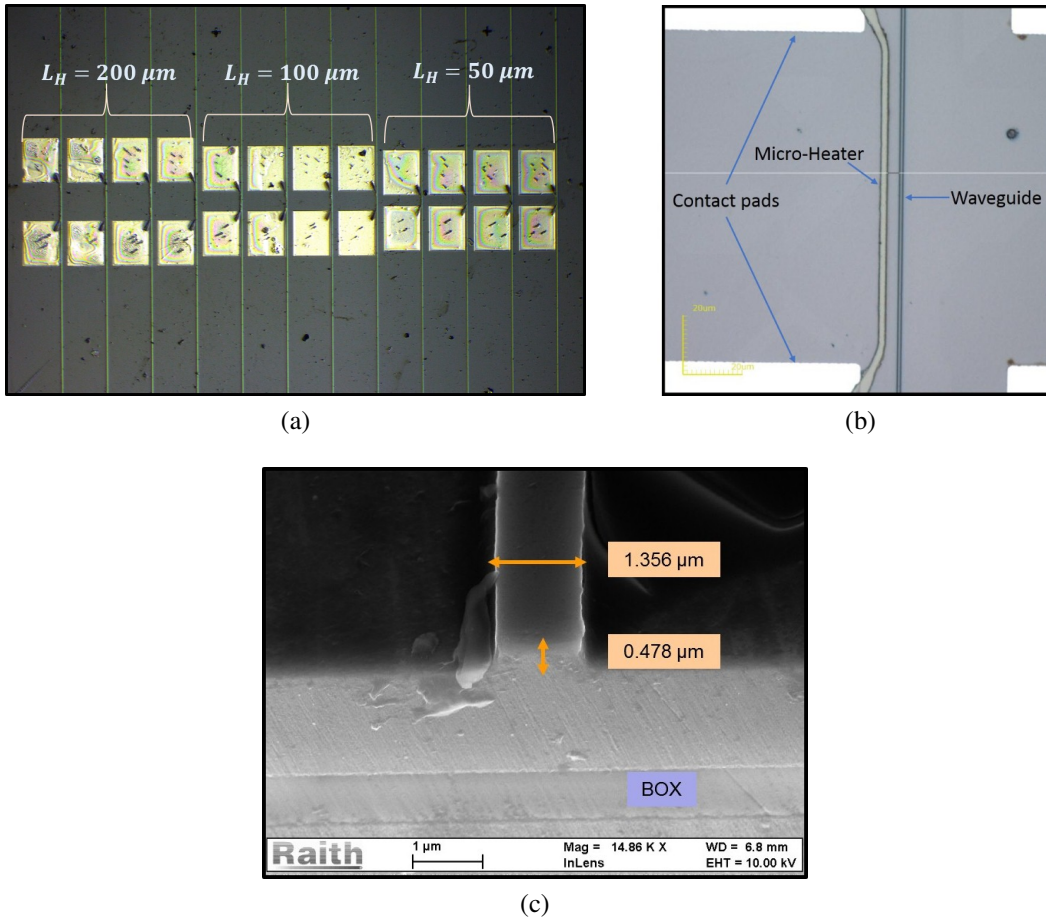


Figure 4.6: (a) Photograph of microheaters of different L_H integrated with rib waveguides. (b) Zoomed Confocal micrograph of a microheater with $L_H = 100 \mu m$, $W_H = 2 \mu m$. (c) SEM image of polished end-facet of waveguide with typical width and etch depth measured. Image clearly shows the cross-section of $2 \mu m$ SOI.

4.2.1 Waveguide Loss and Mode Profile Measurement

Waveguides were characterized using standard free space setup [63]. The device under test (silicon photonics chip) was mounted on a copper substrate holder maintained at room temperature ($\sim 300K$). Input polarization of light from Tunable laser source was fixed by fiber based polarization controller and Glan-Thompson polarizer (P). Polarized

light was focused at the end facet of waveguide by lens assembly comprising of L_1 , L_2 . Output from the waveguide was collimated by lens L_3 and was fed to InGaAs detector. Initially waveguide loss was estimated using Fabry-Perot resonance based loss measurement technique [64]. We consider waveguides as lossy Fabry-Perot cavities with polished end facets acting as reflectors. At Si-air interface, reflectivity R_F of a smooth, vertical interface can be calculated using the Fresnel reflection formula

$$R_F = \left(\frac{n_{\text{eff}} - 1}{n_{\text{eff}} + 1} \right)^2 \quad (4.1)$$

Where n_{eff} is effective index of guided mode. R_F for fabricated waveguides was estimated to be $\sim 30\%$. For a typical Fabry-Perot cavity of length L , throughput transmission of a waveguide, P_{Out} is governed by the well known equation

$$P_{\text{Out}} = \frac{\eta P_{\text{in}} (1 - R_F)^2 e^{-\alpha L}}{(1 - R_F e^{-\alpha L})^2 + 4 R_F e^{-\alpha L} \sin^2(\Delta\phi)} \quad (4.2)$$

Where P_{in} is input power, η is coupling efficiency, α is propagation loss and $\Delta\phi = \Delta\beta L$. Thus, by tuning wavelength one can estimate the loss of the waveguide. Figure 4.7 shows the measured transmission characteristics of a waveguide for TE polarization as a function of wavelength around 1570 nm. Each maxima and minima correspond to constructive and destructive interference inside the cavity. Free spectral range (FSR) defined as difference between each consecutive maxima or minima in the characteristic is given by

$$FSR = \frac{\lambda^2}{2n_g L} \quad (4.3)$$

Where n_g is group index. Propagation loss α is estimated from the extinction ratio ζ where $\zeta = \frac{P_{\text{max}}}{P_{\text{min}}}$, P_{max} corresponds to maximum power when $\Delta\phi$ is 0 or multiples of 2π , similarly P_{min} corresponds to minimum power when $\Delta\phi$ is π . Thus, using Equation 4.2

and measured response (Figure 4.7) one can evaluate α as

$$\alpha = -\frac{1}{L} \ln \left(\frac{1}{R_F} \frac{\sqrt{\zeta} - 1}{\sqrt{\zeta} + 1} \right) \quad (4.4)$$

Using this technique, waveguide loss for some of the best waveguides were estimated

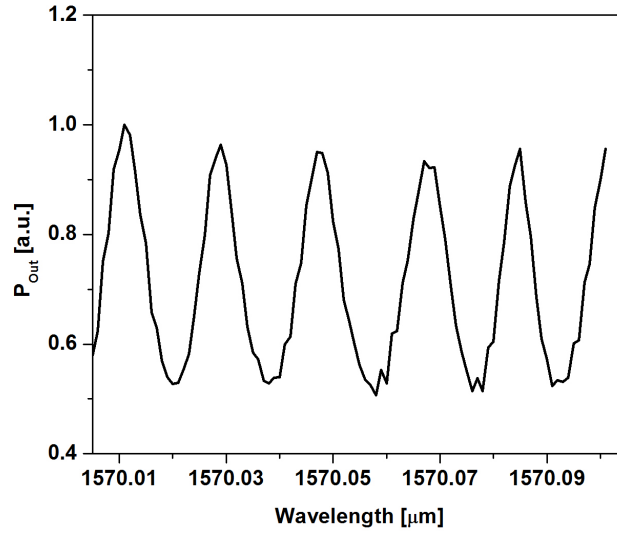


Figure 4.7: Measured normalized transmission characteristics of a waveguide for TE polarization as a function of wavelength around 1570 nm.

to be ~ 0.5 dB/cm (1 dB/cm) for TE (TM) polarization. It is worth mentioning that reflectivity value calculated is for cleaved vertical end facets, but in reality, polished end facets are far from ideal as seen in Figure 4.6c which leads to lower reflectivity. Hence, this technique gives the maximum possible value of α , actual loss will always be less than this value. The excess optical loss in the waveguide due to heater integration has been found to be negligibly small (< 0.2 dB).

Mode profile was measured by replacing the detector at the output of characterization setup (Figure 4.9) with a Charge Coupled Device (CCD) camera. Input power from the laser was reduced to < 0.1 mW, ensuring CCD array is out of saturation. Mode profiles

were recorded for both the polarization and is shown in Figure 4.8. It is evident from profiles that the waveguide supports well confined single mode for both the polarization. Since the waveguide is shallow etched ($h \sim 500$ nm), field distribution is elliptical. Mode sizes were estimated by comparing mode size of a SMF. Measured mode size is $6.1 \mu\text{m} \times 2.6 \mu\text{m}$ and $5.7 \mu\text{m} \times 2.6 \mu\text{m}$ for TE and TM polarization respectively. Lumerical MODE solver was used to calculate the mode size of the waveguide for both TE and TM polarization. Calculated mode size is $5.6 \mu\text{m} \times 1.6 \mu\text{m}$ and $4.2 \mu\text{m} \times 1.5 \mu\text{m}$ for TE and TM polarization respectively. Difference in calculated and measured mode sizes can be attributed to non-vertical sidewalls of waveguide and finite resolution of CCD camera used in mode profile measurement.

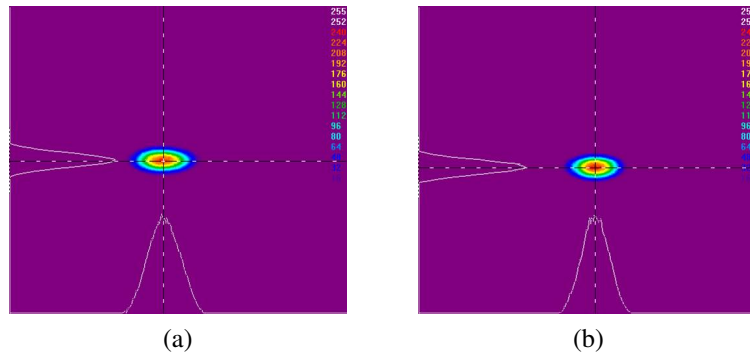


Figure 4.8: (a) Measured Mode profile for TE polarization, Mode size is $6.1 \mu\text{m} \times 2.6 \mu\text{m}$. (b) Measured Mode profile for TM polarization, Mode size is $5.7 \mu\text{m} \times 2.6 \mu\text{m}$

4.2.2 Sheet Resistance Measurement

The sheet resistance for the Titanium thin films used for defining heaters was measured using Four probe method and was found to be $\sim 40 \Omega/\square$, which gives a line resistance (R_l) of $20 \Omega/\mu\text{m}$ ($13.33 \Omega/\mu\text{m}$) for $W_H = 2 \mu\text{m}$ ($3 \mu\text{m}$).

4.3 Results and Discussion

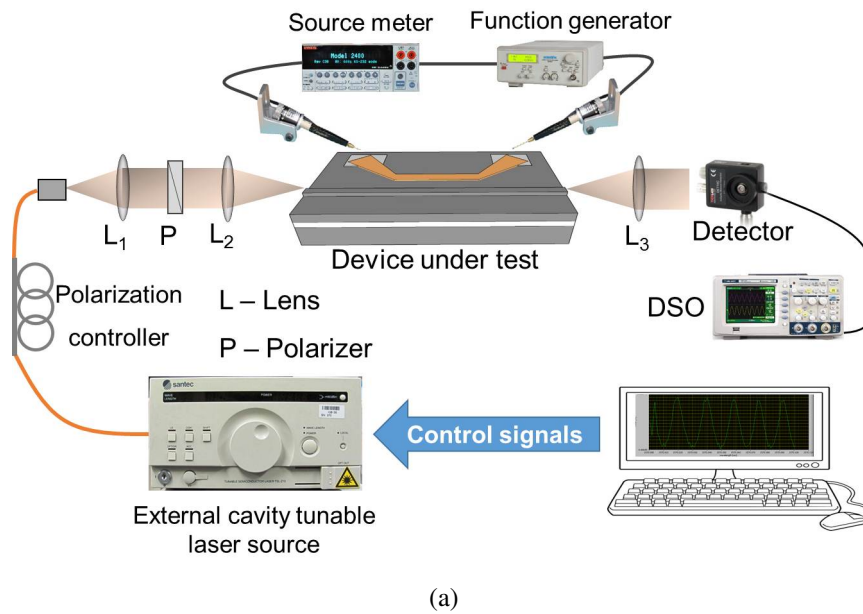
Microheaters integrated with rib waveguides were characterized as per the setup shown in Figure 4.9a, zoomed in photograph of the free space characterization setup used to test the microheaters is shown in Figure 4.9b; DUT along with electrical probes can be seen in the centre along with input and output objective lenses which are controlled by pico actuators.

4.3.1 Static Microheater Response

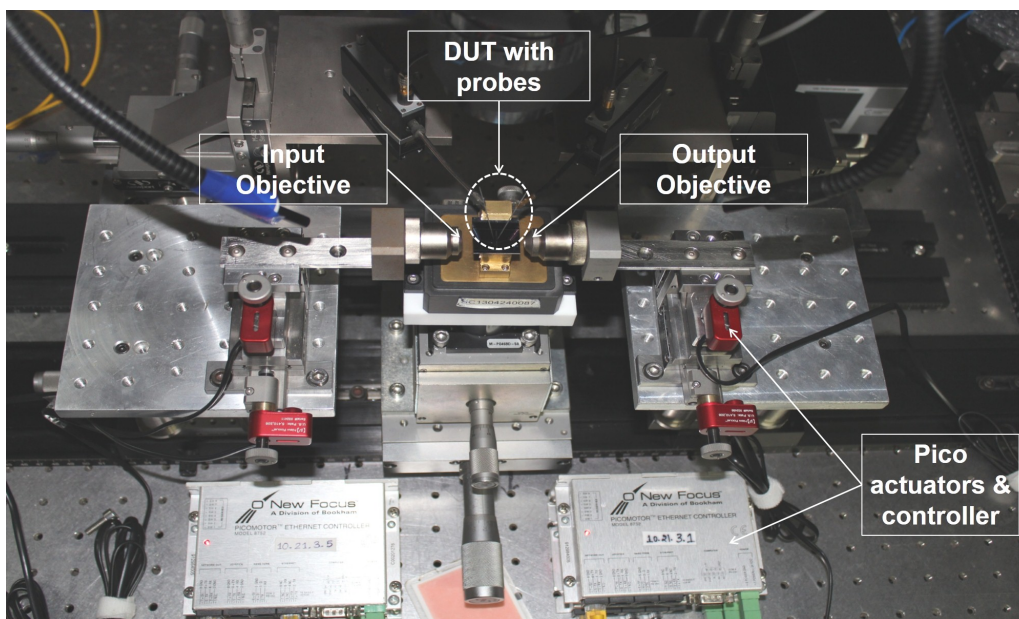
Since the effective heater length is defined by L_{eff} , the effective heater resistance can be quantified as $R_{\text{eff}} = R_l \times L_{\text{eff}}$, which is responsible for uniform temperature rise of $\delta T_p(V_H)$ according to our model Eqns. (3.2) and (3.3). Thus the effective electrical power delivered by the microheater to the waveguide of length L_{eff} is given by:

$$P_{\text{eff}} = i_H^2 \cdot R_l \cdot L_{\text{eff}} \quad (4.5)$$

where, i_H is the current through microheater. This is the power directly responsible for phase change in the waveguide via thermo-optic effect. In other words, P_{eff} takes into account of the power utilized for phase-shift due to edge effects as well. However, actual temperature rise δT_p can be estimated only by the knowledge of phase change ($\Delta\phi$). It must be noted that the resistance of Ti-microheater increases with the increase of its operating temperature, which has been taken into account by considering the temperature coefficient of resistance ($3 \times 10^{-3}/^\circ\text{C}$) for bulk Ti. This is a good assumption as the Ti thin-film thickness ($t_H \sim 150$ nm) used for microheaters is large enough to be considered like bulk as far as resistivity is concerned [65]. We have used Fabry-Perot modulation technique to estimate the P_{eff} for a desired phase change in the waveguide.



(a)



(b)

Figure 4.9: (a) Free space characterization setup used to test microheaters integrated with rib waveguides. (b) Zoomed in photograph of the characterization setup showing DUT with electrical probes at the centre and i/o objective lenses controlled with pico actuators at either side.

First, a resonant wavelength ($\lambda_r \sim 1570$ nm) was launched at the input of the Fabry-Perot cavity of length L (20-mm-long waveguide). Afterwards, a current source meter was connected between heater terminals as shown in Figure 4.9a. The 2-probe configuration is used to source current and measurement of voltage across terminals. The current source is used to drive the microheaters to estimate directly the actual Joule heating power used for changing phase in the waveguide by discounting losses due to Al contact pads. As the current through the heater increases, the induced phase change in the waveguide causes a modulated throughput power given by:

$$P_T = \frac{\eta P_{\text{in}}(1 - R_F)^2 e^{-\alpha L}}{(1 - R_F e^{-\alpha L})^2 + 4R_F e^{-\alpha L} \sin^2(\Delta\phi)} \quad (4.6)$$

where P_{in} is the input power, η is the coupling efficiency, and α is propagation loss of the waveguide. Figure 4.10a shows the calculated Fabry-Perot transmission (TE-polarization) as a function of $\Delta\phi$; whereas, Figure 4.10b shows the measured Fabry-Perot transmission (TE-polarization) as a function of current (in steps of $50 \mu\text{A}$) through the heater with $L_H = 100 \mu\text{m}$. Time step between each reading in individual measurements was 200 ms, ensuring sufficient time for thermal equilibrium to be reached. Similar measurements were also carried out for heaters with $L_H = 50 \mu\text{m}$ and $200 \mu\text{m}$. It is now evident that the phase difference between successive maxima and minima is $\pi/2$. This information allows us to plot P_{eff} vs. $\Delta\phi$ for heaters with three different lengths for both TE and TM polarization for $W_H = 2 \mu\text{m}$ as shown in Figure 4.11a. We observe that the effective power needed for a certain phase change is always lower for a shorter heater length. However, this is achieved only at the cost of higher temperature change in the waveguide as shown in Figure 4.11b. It is worth to mention here that there were thermal drifts observed in Fabry-Perot transmission at reasonably higher operating temperatures of the microheater ($\delta T_p > 150\text{K}$). This may be attributed to the fluctuations in air-assisted heat convection from the waveguide surface. Nevertheless, higher peak

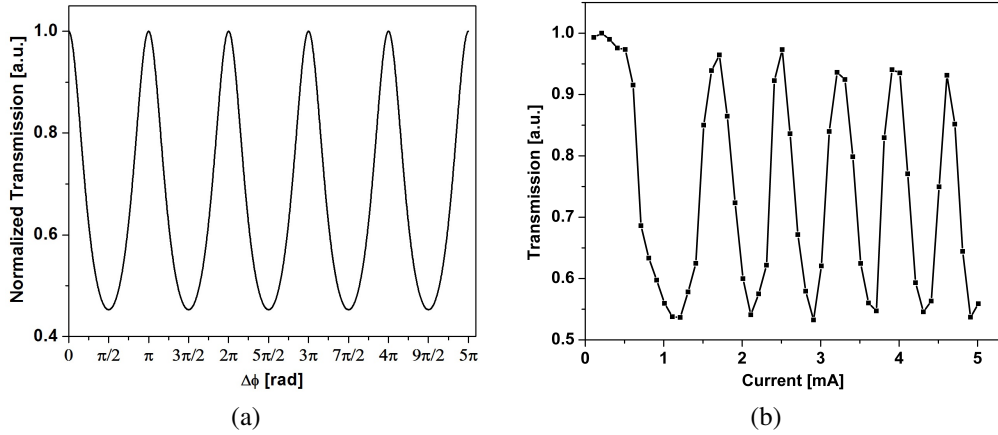


Figure 4.10: (a) Calculated intensity modulated output as function of $\Delta\phi$ for a waveguide cavity of length 20 mm with propagation loss of 1 dB/cm for TE-polarization at $\lambda = 1570$ nm. (b) Experimentally obtained intensity modulated output (TE-polarization at $\lambda = 1570$ nm) as a function of current (i_H) through a heater with $L_H = 100 \mu\text{m}$ and $W_H = 2 \mu\text{m}$.

temperature creates a larger temperature gradient across the guided mode (especially for shorter L_H), eventually leads to thermal stress [66] and may be the reason for polarization dependent performance as seen in Figure 4.11a. The power consumption for TM-polarized light is nearly three times more than that of TE-polarized light in case of $50 \mu\text{m}$ long heater, whereas it is almost equal for $200 \mu\text{m}$ long heater. We also notice that for $100 \mu\text{m}$ long heater, the birefringence is slightly present but but could very well be uncertainty in measurements due to finite step size of current source ($\sim 50 \mu\text{A}$). To study the effect of W_H on P_{eff} for same L_H , similar measurements were carried out for microheaters with $W_H = 3 \mu\text{m}$ as well. As seen in Figure 4.11c, for a given polarization, (shown for TE polarized light) heaters with $W_H = 3 \mu\text{m}$ require higher effective electrical power P_{eff} compared to heaters with $W_H = 2 \mu\text{m}$. Wider heaters tend to heat the surroundings more via the slab thus lot of power is wasted.

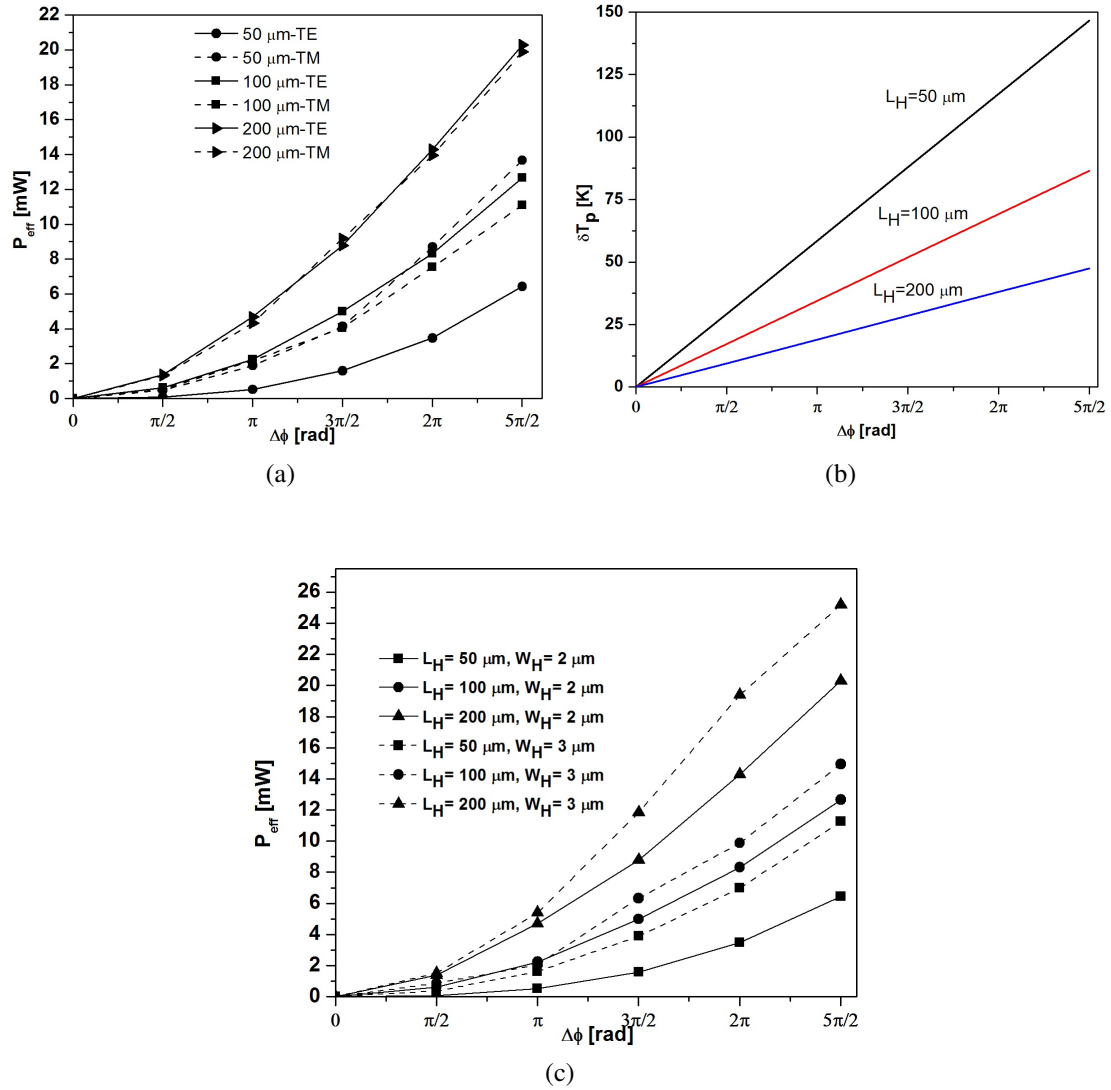


Figure 4.11: (a) Effective electrical power (P_{eff}) versus induced phase change ($\Delta\phi$) in the waveguide for $W_H = 2 \mu\text{m}$, and different L_H viz. $50 \mu\text{m}$, $100 \mu\text{m}$, $200 \mu\text{m}$ for TE (solid line) and TM (dotted line) polarized light. (b) Peak temperature change (δT_p) required as a function of desired phase change of the guided mode. (c) Effective electrical power (P_{eff}) versus induced phase change ($\Delta\phi$) in the waveguide for $W_H = 2 \mu\text{m}$ (solid line) and $W_H = 3 \mu\text{m}$ (dotted line), and different L_H viz. $50 \mu\text{m}$, $100 \mu\text{m}$, $200 \mu\text{m}$ for TE polarized light.

4.3.2 Investigation of Polarization Rotation

Due to asymmetrical configuration of slab deposited microheaters as seen in Figure 3.1, it is worthwhile to investigate whether polarization rotation is observed in waveguides due to slab deposited microheaters. Characterization setup as shown in Figure 4.9a was modified to include a polarizer at the output before the detector to filter a particular polarization. Input polarization of light was maintained by polarization controller and a polarizer with an extinction of ~ 20 dB. First, TE polarized light was focused on one of the reference waveguides and output polarizer was kept to transmit TE polarized light, then output polarizer was rotated to allow TM polarized light and measurements were recorded. It was observed that the reference waveguides maintained the polarization of the input light with extinction ~ 20 dB. Next, input polarized light was focused

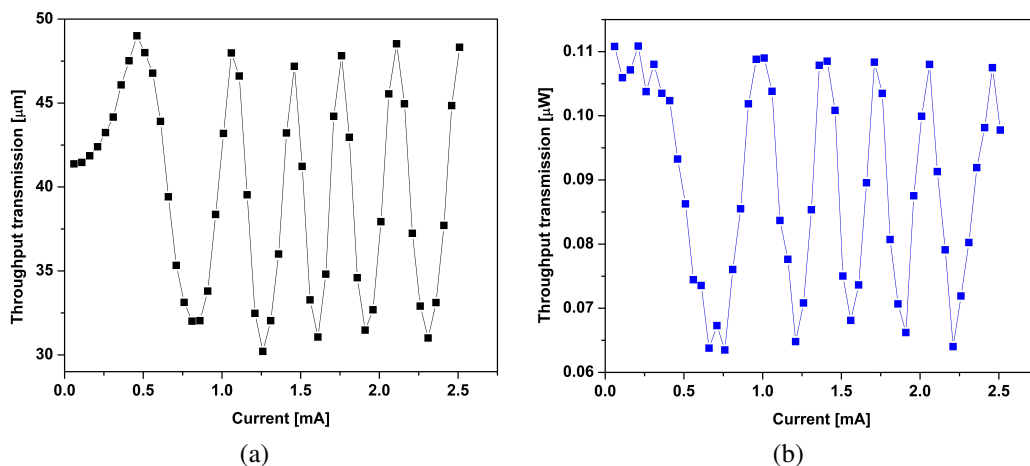


Figure 4.12: Throughput transmission as a function of current of a waveguide with slab deposited microheater with TE polarized light as input: (a) Output polarizer set to pass TE polarized light (b) Output polarizer set to pass TM polarized light.

on waveguide with slab deposited microheater. Input polarization was set to TE and current was supplied to the microheater through the probe pads. Output polarizer was first kept to transmit TE polarization and then TM. Fabry perot oscillations as a function

of current were recorded for the both the cases and is shown in Figure 4.12 a,b. As observed, extinction ratio remains constant for both the polarization as a function of current, indicating there is no polarization rotation taking place in the waveguides due to applied bias on microheater. Moreover, the plots clearly shows that $n_{\text{eff, TE}}$ and $n_{\text{eff, TM}}$ are not equal as FSR is different for TE and TM polarization.

4.3.3 Transient Response

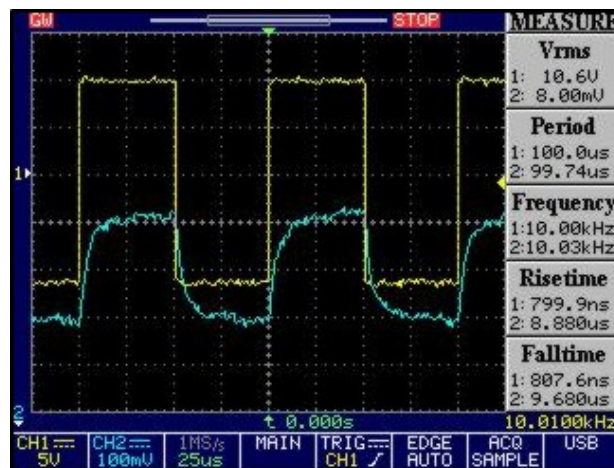


Figure 4.13: Transient response : Measured output response of microheater with $W_H = 2 \mu\text{m}$ and $L_H = 200 \mu\text{m}$ (blue trace) to a 10 kHz drive signal (yellow trace). Average response time is $\tau_{\text{resp}} \sim 9 \mu\text{s}$.

To compare the response time, a 10 kHz small-signal (square pulse with $1 \mu\text{s}$ rise-time) from a function generator riding on top of a fixed DC bias was used to drive the microheaters as shown in Figure 4.9 and the modulated optical throughput power was recorded as a function of time. Figure 4.13 shows a typical transient response recorded in a DSO where blue trace is the output of the micro heater of $L_H = 200 \mu\text{m}$, $W_H = 2 \mu\text{m}$ in response of input drive voltage shown in yellow trace. We did not observe any significant differences in response time for three different lengths ($L_H = 50 \mu\text{m}$, $100 \mu\text{m}$, and $200 \mu\text{m}$) of the microheaters. This is because the difference in

time constant could not be resolved below $1\mu\text{s}$ (limited by the function generator used in the experiment). Average response time is found to be $\tau_{\text{resp}} \sim 9\mu\text{s}$. Thus the effective figure of merit of microheater with $L_H = 50\mu\text{m}$ has been estimated to $P_{\text{eff},\pi} \times \tau_{\text{resp}} \sim 4.5\text{ mW}\cdot\mu\text{s}$, where $P_{\text{eff},\pi}$ is the effective electrical power consumed for a thermo-optic phase-shift of π in the waveguide. The corresponding actual electrical power consumed by the microheater is $P_\pi = 1.1\text{ mW}$.

4.4 Conclusions

Slab deposited microheaters were integrated along rib waveguides on $2\text{-}\mu\text{m}$ SOI. Optimized fabrication process flow was discussed in detail. End fire characterization setup was used to measure loss and mode profile of waveguides for both the polarization. Propagation loss of some of the best waveguides was measured to be $\sim 0.5\text{ dB/cm}$ (1 dB/cm) for TE (TM) polarization. Linear piecewise model discussed in the previous chapter was used to evaluate geometry dependent microheater performance. $P_{\text{eff},\pi}$ was measured to be $\sim 500\mu\text{W}$ for heater length $50\mu\text{m}$. Smaller heaters were found to be more efficient compared to longer heaters. Temperature induced birefringence was observed for smaller heaters. Wider heaters tend to dissipate heat more to the surroundings, hence were observed to be less efficient. Polarization rotation was not observed in waveguides integrated with microheaters. Transient analysis of microheaters was also carried out. Average response time was found to be $\sim 9\mu\text{s}$.

CHAPTER 5

CONCLUSIONS

This chapter summarizes highlights and key take-away points of this thesis. It also discusses the future scope of this work.

5.1 Summary

To assess thermal crosstalk and fabrication induced phase error in reconfigurable circuits in SOI platform; maximally flat delay lines based on Coupled Ring Optical Waveguides (CROWs) is taken as a case study. Design principle employed in extracting inter-ring coupling coefficients for maximally flat delay response is discussed in detail. Fabrication imperfections leads to deleterious response in maximally flat delay lines. Thermo-optic tuning of phase error induced due to fabrication imperfections is discussed. But, thermal crosstalk in these tightly packed large scale circuits is ubiquitous, therefore, a linear piece wise model is formulated to study temperature distribution along the waveguide which is valid for both micron and sub micron waveguides. It is observed that effective heater length has a linear dependence on slab height of rib waveguide. Fabry-Perot modulation technique has been used to characterize the microheaters integrated with single-mode waveguide operating at $\lambda \sim 1550$ nm. The experimental results and the piecewise model have been exploited to compare the length dependent figure of merits of the microheaters. As expected, shorter heater lengths are found to be efficient in terms of electrical power budget - longer heaters dissipate more energy to device layer and substrate. Besides, we observed that higher temperature gradient in

the waveguide causes thermal stress (in the lateral direction of the waveguide) resulting in increased polarization dependencies. It is also observed that narrow heaters are more efficient compared to wider heaters. No polarization rotation was observed in the waveguides due to slab deposited microheaters. Chapter 2 discusses a case study of maximally flat delay lines using Coupled Ring Optical Waveguides (CROWs). Design principle employed in extracting inter-ring coupling coefficients is discussed in detail. Fabrication induced disorder in delay response is also studied. Active tuning of phase error induced due to fabrication imperfection using thermo optic effect is discussed. Thermal crosstalk in these tightly packed large scale circuits is ubiquitous, therefore a detailed study of temperature distribution along the waveguide due to applied bias in slab deposited microheater is undertaken in this chapter. In Chapter 3, A linear piece-wise model is formulated to study temperature distribution along the waveguide which is valid for both micron and sub micron waveguides. Chapter 4 discusses fabrication and characterization of slab deposited microheater on $2\ \mu\text{m}$ SOI. Optimized fabrication processes and parameters are described in detail. Characterization method and the associated results viz. loss and mode profile measurement, static and transient response of microheaters is presented. The effective thermal power budget of $P_{\text{eff},\pi} \sim 500\ \mu\text{W}$ (out of actually consumed power $P_{\pi} = 1.1\ \text{mW}$) for a π phase-shift and a switching time of $\tau \sim 9\ \mu\text{s}$, have been recorded for a typical Ti heater stripe of length $L_H = 50\ \mu\text{m}$, width $W_H = 2\ \mu\text{m}$, and thickness $t_H \sim 150\ \text{nm}$; integrated with a Fabry-Perot waveguide cavity of length $\sim 20\ \text{mm}$.

5.2 Future scope of work

Some of the possible improvements and future scope of work is described below.

1. Temperature induced birefringence observed for shorter heaters need to be investigated in detail.

2. To reduce thermal crosstalk in slab deposited microheaters, air trenches can be used to trap the heat. Linear piecewise model can be modified to incorporate the effect of trenches on temperature distribution along the waveguide.
3. Linear piecewise model can be extended to different heater geometries viz. meander, curved etc.
4. Waveguide loss can be further reduced using ICPRIE instead of conventional RIE for smooth, vertical waveguide sidewalls.
5. With nano-fabrication and nano-characterization facilities at disposal, it is feasible to realize microheaters integrated with sub micron waveguides. Thus enabling compact reconfigurable circuits viz. delay lines, routers etc.

APPENDIX A

FABRICATION CHEMISTRY

A.1 Chromium Etchant

Chromium Etchant is a solution of Ammonium Ceric Nitrate (ACN) crystals and acetic acid. Steps for preparing the etchant are listed below:

1. 8 g ACN in 30 ml DI water, solution should be stirred continuously to dissolve the crystals completely.
2. 3 ml Acetic acid dissolved in 35 ml DI water.
3. Mix 2 parts of the solution with one part DI water to get the Cr etchant solution.

A.2 Aluminum Etchant

Aluminum etchant is an Orthophosphoric acid based solution. Steps for preparing the etchant are as follows:

1. 77 ml of H_3PO_4 is mixed with 5 ml of DI water.
2. 15 ml of CH_3COOH is mixed with 3 ml of HNO_3
3. Finally, two solutions are mixed together to get 100 ml Al etchant solution.

REFERENCES

- [1] L.-W. Luo, N. Ophir, C. P. Chen, L. H. Gabrielli, C. B. Poitras, K. Bergmen, and M. Lipson, “Wdm-compatible mode-division multiplexing on a silicon chip,” *Nature communications*, vol. 5, 2014.
- [2] F. Horst, W. M. Green, S. Assefa, S. M. Shank, Y. A. Vlasov, and B. J. Offrein, “Cascaded mach-zehnder wavelength filters in silicon photonics for low loss and flat pass-band wdm (de-) multiplexing,” *Optics express*, vol. 21, no. 10, pp. 11652–11658, 2013.
- [3] H. Qiu, G. Jiang, T. Hu, H. Shao, P. Yu, J. Yang, and X. Jiang, “Fsr-free add-drop filter based on silicon grating-assisted contradirectional couplers,” *Optics letters*, vol. 38, no. 1, pp. 1–3, 2013.
- [4] J. Capmany, D. Domenech, and P. Muñoz, “Silicon graphene waveguide tunable broadband microwave photonics phase shifter,” *Optics express*, vol. 22, no. 7, pp. 8094–8100, 2014.
- [5] E. Marchena, T. Creazzo, S. B. Krasulick, P. Yu, D. Van Orden, J. Y. Spann, C. C. Blivin, J. M. Dallesasse, P. Varangis, R. J. Stone, *et al.*, “Integrated tunable cmos laser for si photonics,” in *Optical Fiber Communication Conference*, pp. PDP5C–7, Optical Society of America, 2013.
- [6] R. E. Camacho-Aguilera, Y. Cai, N. Patel, J. T. Bessette, M. Romagnoli, L. C. Kimerling, and J. Michel, “An electrically pumped germanium laser,” *Optics express*, vol. 20, no. 10, pp. 11316–11320, 2012.
- [7] G. C. Park, W. Xue, A. Taghizadeh, E. Semenova, K. Yvind, J. Mørk, and I.-S. Chung, “Hybrid vertical-cavity laser with lateral emission into a silicon waveguide,” *Laser & Photonics Reviews*, vol. 9, no. 3, pp. L11–L15, 2015.
- [8] X. Wang, Z. Cheng, K. Xu, H. K. Tsang, and J.-B. Xu, “High-responsivity graphene/silicon-heterostructure waveguide photodetectors,” *Nature Photonics*, vol. 7, no. 11, pp. 888–891, 2013.
- [9] D. J. Thomson, F. Y. Gardes, J.-M. Fedeli, S. Zlatanovic, Y. Hu, B. P. P. Kuo, E. Myslivets, N. Alic, S. Radic, G. Z. Mashanovich, *et al.*, “50-gb/s silicon optical modulator,” *Photonics Technology Letters, IEEE*, vol. 24, no. 4, pp. 234–236, 2012.

- [10] V. J. Sorger, N. D. Lanzillotti-Kimura, R.-M. Ma, and X. Zhang, “Ultra-compact silicon nanophotonic modulator with broadband response,” *Nanophotonics*, vol. 1, no. 1, pp. 17–22, 2012.
- [11] S. Srinivasan, R. Moreira, D. Blumenthal, and J. E. Bowers, “Design of integrated hybrid silicon waveguide optical gyroscope,” *Optics express*, vol. 22, no. 21, pp. 24988–24993, 2014.
- [12] J. G. Wangüemert-Pérez, P. Cheben, A. Ortega-Moñux, C. Alonso-Ramos, D. Pérez-Galacho, R. Halir, I. Molina-Fernández, D.-X. Xu, and J. H. Schmid, “Evanescent field waveguide sensing with subwavelength grating structures in silicon-on-insulator,” *Optics letters*, vol. 39, no. 15, pp. 4442–4445, 2014.
- [13] E. Ryckeboer, A. Gassenq, M. Muneeb, N. Hattasan, S. Pathak, L. Cerutti, J. Rodriguez, E. Tournie, W. Bogaerts, R. Baets, *et al.*, “Silicon-on-insulator spectrometers with integrated gainassb photodiodes for wide-band spectroscopy from 1510 to 2300 nm,” *Optics express*, vol. 21, no. 5, pp. 6101–6108, 2013.
- [14] C. Sun, M. T. Wade, Y. Lee, J. S. Orcutt, L. Alloatti, M. S. Georgas, A. S. Waterman, J. M. Shainline, R. R. Avizienis, S. Lin, *et al.*, “Single-chip microprocessor that communicates directly using light,” *Nature*, vol. 528, no. 7583, pp. 534–538, 2015.
- [15] Y. Vlasov *et al.*, “Silicon CMOS-integrated nano-photonics for computer and data communications beyond 100G,” *Communications Magazine, IEEE*, vol. 50, no. 2, pp. s67–s72, 2012.
- [16] M. Hochberg and T. Baehr-Jones, “Towards fabless silicon photonics,” *Nature Photonics*, vol. 4, no. 8, pp. 492–494, 2010.
- [17] R. Soref, “Silicon photonics: a review of recent literature,” *Silicon*, vol. 2, no. 1, pp. 1–6, 2010.
- [18] P. Dumon, W. Bogaerts, R. Baets, J.-M. Fedeli, and L. Fulbert, “Towards foundry approach for silicon photonics: silicon photonics platform epixfab,” *Electronics letters*, vol. 45, no. 12, pp. 581–582, 2009.
- [19] J. S. Orcutt, A. Khilo, C. W. Holzwarth, M. A. Popović, H. Li, J. Sun, T. Bonifield, R. Hollingsworth, F. X. Kärtner, H. I. Smith, *et al.*, “Nanophotonic integration in state-of-the-art CMOS foundries,” *Optics Express*, vol. 19, no. 3, pp. 2335–2346, 2011.
- [20] B. Jalali and S. Fathpour, “Silicon photonics,” *Lightwave Technology, Journal of*, vol. 24, no. 12, pp. 4600–4615, 2006.

- [21] G. T. Reed, G. Mashanovich, F. Gardes, and D. Thomson, "Silicon optical modulators," *Nature photonics*, vol. 4, no. 8, pp. 518–526, 2010.
- [22] A. Liu, R. Jones, L. Liao, D. Samara-Rubio, D. Rubin, O. Cohen, R. Nicolaescu, and M. Paniccia, "A high-speed silicon optical modulator based on a metal–oxide–semiconductor capacitor," *Nature*, vol. 427, no. 6975, pp. 615–618, 2004.
- [23] Y. Vlasov, W. M. Green, and F. Xia, "High-throughput silicon nanophotonic wavelength-insensitive switch for on-chip optical networks," *nature photonics*, vol. 2, no. 4, pp. 242–246, 2008.
- [24] P. Sun and R. M. Reano, "Submilliwatt thermo-optic switches using free-standing silicon-on-insulator strip waveguides," *Optics express*, vol. 18, no. 8, pp. 8406–8411, 2010.
- [25] N. C. Harris, Y. Ma, J. Mower, T. Baehr-Jones, D. Englund, M. Hochberg, and C. Galland, "Efficient, compact and low loss thermo-optic phase shifter in silicon," *Optics express*, vol. 22, no. 9, pp. 10487–10493, 2014.
- [26] J. Song, Q. Fang, S. Tao, T. Liow, M. Yu, G. Lo, and D. Kwong, "Fast and low power michelson interferometer thermo-optical switch on SOI," *Optics express*, vol. 16, no. 20, pp. 15304–15311, 2008.
- [27] H. Zhou, J. Song, E. K. Chee, C. Li, H. Zhang, and G. Lo, "A compact thermo-optical multimode-interference silicon-based 1×4 nano-photonic switch," *Optics express*, vol. 21, no. 18, pp. 21403–21413, 2013.
- [28] K. Suzuki, K. Tanizawa, T. Matsukawa, G. Cong, S.-H. Kim, S. Suda, M. Ohno, T. Chiba, H. Tadokoro, M. Yanagihara, *et al.*, "Ultra-compact 8×8 strictly-non-blocking Si-wire PILOSS switch," *Optics express*, vol. 22, no. 4, pp. 3887–3894, 2014.
- [29] X. Zheng, I. Shubin, G. Li, T. Pinguet, A. Mekis, J. Yao, H. Thacker, Y. Luo, J. Costa, K. Raj, *et al.*, "A tunable 1×4 silicon CMOS photonic wavelength multiplexer/demultiplexer for dense optical interconnects," *Optics express*, vol. 18, no. 5, pp. 5151–5160, 2010.
- [30] R. Aguinaldo, A. Forencich, C. DeRose, A. Lentine, D. C. Trotter, Y. Fainman, G. Porter, G. Papen, and S. Mookherjea, "Wideband silicon-photonic thermo-optic switch in a wavelength-division multiplexed ring network," *Optics express*, vol. 22, no. 7, pp. 8205–8218, 2014.
- [31] P. Dong, W. Qian, H. Liang, R. Shafiq, D. Feng, G. Li, J. E. Cunningham, A. V. Krishnamoorthy, and M. Asghari, "Thermally tunable silicon racetrack resonators

- with ultralow tuning power,” *Optics express*, vol. 18, no. 19, pp. 20298–20304, 2010.
- [32] P. Dong, W. Qian, H. Liang, R. Shafiq, N.-N. Feng, D. Feng, X. Zheng, A. V. Krishnamoorthy, and M. Asghari, “Low power and compact reconfigurable multiplexing devices based on silicon microring resonators,” *Optics express*, vol. 18, no. 10, pp. 9852–9858, 2010.
- [33] W. S. Fegadolli, L. Feng, M. M.-U. Rahman, J. E. Oliveira, V. R. Almeida, and A. Scherer, “Experimental demonstration of a reconfigurable silicon thermo-optical device based on spectral tuning of ring resonators for optical signal processing,” *Optics express*, vol. 22, no. 3, pp. 3425–3431, 2014.
- [34] F. Morichetti, A. Melloni, C. Ferrari, and M. Martinelli, “Error-free continuously-tunable delay at 10 Gbit/s in a reconfigurable on-chip delay-line,” *Optics express*, vol. 16, no. 12, pp. 8395–8405, 2008.
- [35] J. Xie, L. Zhou, Z. Li, J. Wang, and J. Chen, “Seven-bit reconfigurable optical true time delay line based on silicon integration,” *Optics express*, vol. 22, no. 19, pp. 22707–22715, 2014.
- [36] P. Dong, N.-N. Feng, D. Feng, W. Qian, H. Liang, D. C. Lee, B. Luff, T. Banwell, A. Agarwal, P. Toliver, *et al.*, “GHz-bandwidth optical filters based on high-order silicon ring resonators,” *Optics express*, vol. 18, no. 23, pp. 23784–23789, 2010.
- [37] M. H. Khan, H. Shen, Y. Xuan, L. Zhao, S. Xiao, D. E. Leaird, A. M. Weiner, and M. Qi, “Ultrabroad-bandwidth arbitrary radiofrequency waveform generation with a silicon photonic chip-based spectral shaper,” *Nature Photonics*, vol. 4, no. 2, pp. 117–122, 2010.
- [38] M. R. Watts, J. Sun, C. DeRose, D. C. Trotter, R. W. Young, and G. N. Nielson, “Adiabatic thermo-optic Mach–Zehnder switch,” *Optics letters*, vol. 38, no. 5, pp. 733–735, 2013.
- [39] A. Atabaki, E. Shah Hosseini, A. Eftekhari, S. Yegnanarayanan, and A. Adibi, “Optimization of metallic microheaters for high-speed reconfigurable silicon photonics,” *Optics express*, vol. 18, no. 17, pp. 18312–18323, 2010.
- [40] A. Masood, M. Pantouvaki, D. Goossens, G. Lepage, P. Verheyen, J. Van Campenhout, P. Absil, D. Van Thourhout, and W. Bogaerts, “Fabrication and characterization of CMOS-compatible integrated tungsten heaters for thermo-optic tuning in silicon photonics devices,” *Optical Materials Express*, vol. 4, no. 7, pp. 1383–1388, 2014.

- [41] J. Van Campenhout, W. M. Green, S. Assefa, and Y. A. Vlasov, "Integrated NiSi waveguide heaters for CMOS-compatible silicon thermo-optic devices," *Optics letters*, vol. 35, no. 7, pp. 1013–1015, 2010.
- [42] M. Iodice, G. Mazzi, and L. Sirleto, "Thermo-optical static and dynamic analysis of a digital optical switch based on amorphous silicon waveguide," *Optics express*, vol. 14, no. 12, pp. 5266–5278, 2006.
- [43] K. Cui, Q. Zhao, X. Feng, Y. Huang, Y. Li, D. Wang, and W. Zhang, "Thermo-optic switch based on transmission-dip shifting in a double-slot photonic crystal waveguide," *Applied Physics Letters*, vol. 100, no. 20, p. 201102, 2012.
- [44] K. Cui, X. Feng, Y. Huang, Q. Zhao, Z. Huang, and W. Zhang, "Broadband switching functionality based on defect mode coupling in w2 photonic crystal waveguide," *Applied Physics Letters*, vol. 101, no. 15, pp. 151110–151110, 2012.
- [45] A. H. Atabaki, A. A. Eftekhari, S. Yegnanarayanan, and A. Adibi, "Sub-100-nanosecond thermal reconfiguration of silicon photonic devices," *Optics express*, vol. 21, no. 13, pp. 15706–15718, 2013.
- [46] Q. Zhao, K. Cui, X. Feng, F. Liu, W. Zhang, and Y. Huang, "Variable optical attenuator based on photonic crystal waveguide with low-group-index tapers," *Appl. Opt.*, vol. 52, pp. 6245–6249, Sep 2013.
- [47] Q. Zhao, K. Cui, Z. Huang, X. Feng, D. Zhang, F. Liu, W. Zhang, and Y. Huang, "Compact thermo-optic switch based on tapered w1 photonic crystal waveguide," *Photonics Journal, IEEE*, vol. 5, no. 2, pp. 2200606–2200606, 2013.
- [48] D. K. Hunter, M. C. Chia, and I. Andonovic, "Buffering in optical packet switches," *Journal of Lightwave Technology*, vol. 16, no. 12, pp. 2081–2094, 1998.
- [49] R. S. Tucker, P.-C. Ku, and C. J. Chang-Hasnain, "Slow-light optical buffers: capabilities and fundamental limitations," *Journal of Lightwave Technology*, vol. 23, no. 12, p. 4046, 2005.
- [50] A. Melloni, A. Canciamilla, C. Ferrari, F. Morichetti, L. O'Faolain, T. Krauss, R. De La Rue, A. Samarelli, and M. Sorel, "Tunable delay lines in silicon photonics: coupled resonators and photonic crystals, a comparison," *Photonics Journal, IEEE*, vol. 2, no. 2, pp. 181–194, 2010.
- [51] T. Baba, "Slow light in photonic crystals," *Nature Photonics*, vol. 2, no. 8, pp. 465–473, 2008.
- [52] F. Xia, L. Sekaric, and Y. Vlasov, "Ultracompact optical buffers on a silicon chip," *Nature Photonics*, vol. 1, no. 1, pp. 65–71, 2006.

- [53] A. Yariv, “Universal relations for coupling of optical power between microresonators and dielectric waveguides,” *Electronics Letters*, vol. 36, no. 4, pp. 321–322, 2000.
- [54] C. K. Madsen and J. H. Zhao, *Optical filter design and analysis: a signal processing approach*. Wiley, 2001.
- [55] R. Schaumann, H. Xiao, and V. V. Mac, *Design of Analog Filters 2nd Edition*. Oxford University Press, Inc., 2009.
- [56] L. Storch, “Synthesis of constant-time-delay ladder networks using bessel polynomials,” *Proceedings of the IRE*, vol. 42, no. 11, pp. 1666–1675, 1954.
- [57] S. K. Mitra, *Digital signal processing: a computer-based approach*, vol. 1221. McGraw-Hill New York, 2011.
- [58] S. K. Selvaraja, P. De Heyn, G. Winroth, P. Ong, G. Lepage, C. Cailler, A. Rigny, K. Bourdelle, D. VanThourhout, J. Van Campenhout, *et al.*, “Highly uniform and low-loss passive silicon photonics devices using a 300mm CMOS platform,” in *Optical Fiber Communication Conference*, pp. Th2A–33, Optical Society of America, 2014.
- [59] P. Orlandi, F. Morichetti, M. J. Strain, M. Sorel, A. Melloni, and P. Bassi, “Tunable silicon photonics directional coupler driven by a transverse temperature gradient,” *Optics letters*, vol. 38, no. 6, pp. 863–865, 2013.
- [60] C. T. DeRose, N. J. Martinez, R. D. Kekatpure, W. A. Zortman, A. L. Starbuck, A. Pomerene, and A. L. Lentine, “Thermal crosstalk limits for silicon photonic dwdm interconnects,” in *Optical Interconnects Conference, 2014 IEEE*, pp. 125–126, May 2014.
- [61] G. R. Bhatt, R. Sharma, U. Karthik, and B. K. Das, “Dispersion-free SOI interleaver for DWDM applications,” *Journal of Lightwave Technology*, vol. 30, no. 1, pp. 140–146, 2012.
- [62] G. Bhatt and B. K. Das, “Improvement of polarization extinction in silicon waveguide devices,” *Optics Communications*, vol. 285, no. 8, pp. 2067–2070, 2012.
- [63] R. K. Navalakhe, N. DasGupta, and B. K. Das, “Fabrication and characterization of straight and compact s-bend optical waveguides on a silicon-on-insulator platform,” *Applied optics*, vol. 48, no. 31, pp. G125–G130, 2009.
- [64] G. T. Reed and A. P. Knights, *Silicon photonics: an introduction*. John Wiley & Sons, 2004.

- [65] B. Singh and N. Surplice, "The electrical resistivity and resistance-temperature characteristics of thin titanium films," *Thin Solid Films*, vol. 10, no. 2, pp. 243 – 253, 1972.
- [66] M. Huang and X. Yan, "Thermal-stress effects on the temperature sensitivity of optical waveguides," *JOSA B*, vol. 20, no. 6, pp. 1326–1333, 2003.

LIST OF PAPERS BASED ON THESIS

Journal

1. Saket Kaushal, B.K. Das, "Modelling and Experimental Investigation of an Integrated Optical Microheater in SOI," *Applied Optics* vol. 55, no. 11, pp. 2837-2842, 2016.

Conferences

1. Saket Kaushal, B.K. Das, "Design of maximally flat delay lines using apodized CROW structure in SOI", 12th International Conference on Fibre Optics and Photonics, Kharagpur, India , 13-16 December 2014 (Paper- T4B.3)
2. B. K. Das, S. Chandran, R. Sidharth, S. Kaushal, and P. Sah, "Nanoscale Tolerance for Silicon Optical Interconnect Devices", National Conference on Nanoscience and Nanotechnology (NSNT - 2014), 18-19 September 2014, CRNN, University of Calcutta, Kolkata (Invited Talk)
3. B. K. Das, S. Chandran and S. Kaushal, "Optical Interconnect devices with scalable waveguide cross-sections in SOI platform," ICOL-2014, Dehradun, India, 5-8 March 2014 (Invited Talk)
4. Sujith Chandran, Saket Kaushal and B.K. Das, "Monolithic integration of micron to submicron waveguides with 2D mode-size converters in SOI platform" (Invited Talk), SPIE Photonics West 2014, San Francisco, CA, USA, 1-6 February 2014